CHARACTERIZATION OF SEABED GEOMETRY IN A FREE SURFACE WAVE ENVIRONMENT

A Thesis

Presented in Partial Fulfillment of the Requirements for

the Degree Bachelor of Science with Distinction in the

College of Engineering of The Ohio State University

By

Gary R. Margelowsky

* * * * *

The Ohio State University

2008

Honors Examination Committee:

Diane L. Foster, Co-Adviser

Ethan Kubatko, Co-Adviser

Approved by

Co-Adviser

Co-Adviser

Department of Civil and Environmental Engineering and Geodetic Science

ABSTRACT

This specific investigation focuses on bed state variability and bed state evolution influenced by free surface gravity waves. Observations of seabed geometry were obtained at the O. H. Hinsdale Wave Research Laboratory large scale wave flume at Oregon State University in 2005. Flow field and seabed geometry data was collected using a submersible Particle Image Velocimetry (PIV) system. Sea bed geometry measurements include: ripple height (η), wavelength (λ), and radius of curvature (RC). The seabed is determined by the centroid of the maximum light reflection captured by a submerged camera when the bed is illuminated by a laser sheet in the PIV system. Observations were obtained under random wave conditions using a TMA spectrum with significant wave heights ranging from 30 to 50 cm and wave periods in the range of 4 to 8 seconds. The resulting bed geometries ranged from flat to rippled. Over temporal scales as short as one wave period, significant transformations in geometry were recorded. Bedform ripple height was found to be dependent on root-mean-square velocity for wave peak periods of 6 and 8 seconds, and independent of root-mean-square velocity for relatively small peak periods of 4 seconds. Radius of curvature was found to increase with increasing root-mean-square velocity, especially under larger wave height conditions ($H_{mo} = 50$ cm). Finally, bedform wavelength revealed no trends with root-mean-square velocity, wave peak period, or significant wave height.

This is dedicated to my family and friends

TABLE OF CONTENTS

Page

LIST OF TABLES

Table **Page**

LIST OF FIGURES

CHAPTER 1

INTRODUCTION

1.1 Motivation

The nearshore zone within the continental shelf marks an interesting yet complex region that exhibits a wide variety of physical phenomenon. Among these phenomenon are sediment transport and bed state evolution. Although numerous sediment transport studies have occurred, the mechanics of the sea bed are not completely understood. It is accepted, and easily proved, that oscillatory flows generate ripples on a movable sediment bed. However, an established model to predict ripple geometries resulting from fluid-sediment interactions is yet to exist. A comprehensive understanding of the sea bed is imperative for scientific reasons including, but not limited to: boundary layer flow, sediment transport, and wave energy dissipation calculations. Expanding technical knowledge in nearshore processes has practical applications as well. Ripples in the seabed dissipate energy as waves propagate along the ocean towards the shore. Understanding energy dissipation due to bottom roughness, will affect our ability to resolve the impact of storm waves on our coast. According the U.S. Census Bureau, 155.2 million people in the United States lived in a coastal county in 2005 and "Since 1970, the coastal counties share of the population has remained at a relatively stable 53-54%" (U.S. Census Bureau). Significant offshore sediment transport affects

the tourism industry by adversely impacting the size and quality of beaches. Replenishing the sand on these popular tourist destinations, known as beach nourishment, is one way to combat the effects of erosion. Given that beach nourishment averages a minimum cost of $1 million per mile, understanding sediment transport is also important from an economic standpoint. Scientists and engineers must achieve a more comprehensive understanding of fluid-sediment interactions and bed state characteristics. Eventually, an in depth knowledge of small scale processes, such as wave-current boundary layers, vortex generation and ejection, and sediment transport, will also help us to understand large scale coastline behavior such as shoreline erosion and accretion. In the case of wave current boundary layers, the interactions are complex as the boundary layer thickness is a function of the often changing ripple geometry as well as the hydrodynamic forces. The geometry of the seabed directly influences the formation and ejection of vorticites, suspending sediment into the water column. The suspended sediment will likely be carried offshore or onshore, resulting in shoreface erosion or accretion, respectively.

1.2 Literature Review

In 1976, Clifton developed a conceptual model to classify and predict the effects of shoaling waves on sedimentary structures. Empirical formulations were drawn from detailed observations made on the rough waters off the coast of southern Oregon, the relatively calm southeastern coast of Spain, and the protected sandy shores of Willapa Bay, Washington. Fluid density and kinematic viscosity were held constant to reduce the number of independent variables considered. The conceptual model was simplified by neglecting mean flows and beach slope, and waves were assumed to be shore normal with uniform height and period. Thus, after simplifications are made, the bed configuration is a function of wave height (H),

wave period (T), water depth (h), and grain diameter (D). This model is based on the following four parameters: maximum orbital velocity (u_m), velocity asymmetry (Δu_m), median grain size (D), and wave period (T). The effort characterized the following four transport regimes: no sediment movement, symmetric bedforms, asymmetric bedforms, and flatbed (i.e. sheet flow). Asymmetric bedforms could only be described in qualitative terms, and were not included in the empirical model. Characteristics of the symmetric bedform regime were quantified and categorized into three ripple classification schemes, namely: "orbital", "suborbital", and "anorbital". The ripple types are defined by their relations of ripple wave length (λ) to median grain size (D) and maximum orbital velocity (u_m) at a given constant wave period. Maximum orbital wave velocity (u_m) is related to the diameter of wave orbital motion ($2A$) by:

$$u_m = \frac{(2A)\pi}{T} \tag{1.1}$$

Note, wave orbital diameter $2A$ is also denoted d_0. "Orbital" ripples have wavelengths that depend directly on the orbital diameter length, while "suborbital" ripple wavelengths increase with increasing grain size and inversely with orbital diameter, and "anorbital" ripple wavelengths depend solely on grain size.

The resulting model yields a relationship for ripple geometry that is a function of the wave orbital diameter ($2A$) normalized by the grain size (D), and ripple wavelength (λ) normalized by the square root of the grain size ($D^{1/2}$), for symmetric ripples (Figure 1.1). Orbital ripples were found to have $(2A)/D$ values less than 2000, however, for finer grains, $(2A)/D$ does not exceed 1000. Orbital ripple classification data is presented in Table 1.1. Orbital ripple wavelength (λ_{orb}) is calculated as follows:

$$\lambda_{orb} = 0.8(2A) \tag{1.2}$$

Anorbital ripples have a $(2A)/D$ value of greater than 5000, and the ripple length (λ_{ano}) can be calculated through its relationship with grain size:

$$\lambda_{ano} = 60D^{1/2} \tag{1.3}$$

The characteristics of anorbital ripples are represented in Table 1.2. Suborbital ripples are less easily defined, and fall between the categories of orbital and anorbital. Suborbital ripples have a $(2A)/D$ value of greater than 2000 but less than 5000. When finer grains are present, suborbital ripples are found to have a $(2A)/D$ ratio between 1000 and 5000. The common maximum value of 5000 for the ratio $(2A)/D$ in the suborbital ripple class signifies that suborbital ripples are independent of grain size as wave orbital diameter $(2A)$ increases. Characteristics defining ripples as suborbital are depicted in Table 1.3.

Table 1.1: Orbital ripple regime characteristics

Reference	***Observations***	***Relationship***	***Comments***
Clifton (1976)	field	$(2A)/D < 2000$	coarse grains
		$(2A)/D < 1000$	fine grains
		$\lambda_{orb} = 0.8(2A)$	
Clifton and Dingler (1984)	field and laboratory	$100 < (2A)/D < 3000+$	
		$100 < \lambda_{orb}/D < 2000$	
Wiberg and Harris (1994)	field and laboratory	$\lambda_{orb} = 0.62(2A)$	
		$(\eta/\lambda_{orb}) = 0.17$	

Following Clifton (1976), many have analyzed various field and laboratory data sets to test the validity of this model. Similarly, geometry characteristics of symmetric ripple regimes are identified and categorized as orbital, anorbital, and suborbital. The studies following Clifton (1976) include a variety of data sets comprised of observations obtained both in

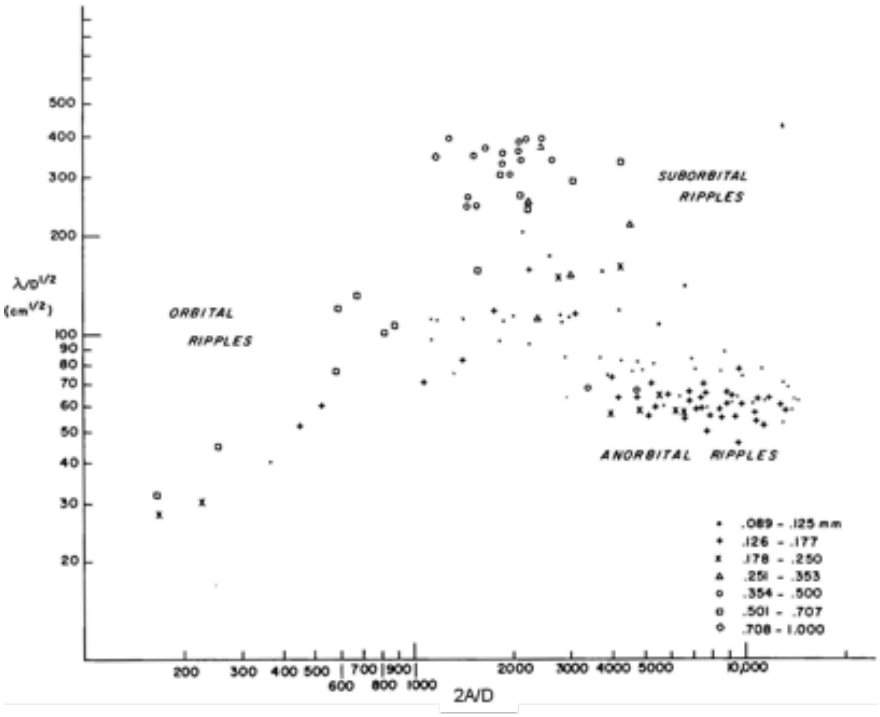

Figure 1.1: Relationship between the normalized wave orbital diameter and ripple wavelength for symmetric ripples. Figure adapted from Clifton (1976)

the laboratory and the field. Clifton and Dingler (1984) found that over a large data set, including both laboratory and field data, the ranges for wave orbital diameter normalized by grain size ($(2A)/D$) and wavelength normalized by grain size (λ/D) for the orbital ripple class extends into a larger range than what was found by Clifton (1976). According to Clifton and Dingler (1984), the ratio of wave orbital diameter over grain size ($2A/D$) is unconcerned with coarse or fine grains (contrary to Clifton (1976)), and extends to values of 3000 or more. This new value is significantly higher than the previously determined value of 2000 for coarse grains and 1000 for fine grains. Clifton and Dingler (1984) also amend the earlier Clifton (1976) model by introducing 100 as a floor value to this relationship. They make further claims about the orbital ripple class by quantifying the orbital wavelength normalized by

Table 1.2: Anorbital ripple regime characteristics

Reference	***Observations***	***Relationship***	***Comments***
Clifton (1976)	field	$(2A)/D > 5000$	
		$\lambda_{ano} = 60D^{1/2}$	
Clifton and Dingler (1984)	field and laboratory	$(2A)/D > 5000$	
		$400 < \lambda_{ano}/D < 600$	
Wiberg and Harris (1994)	field and laboratory	$\lambda_{ano} = 535D$	
		$(\eta/\lambda)_{ano} \approx 0.12$	

Table 1.3: Suborbital ripple regime characteristics

Reference	***Observations***	***Relationship***	***Comments***
Clifton (1976)	field	$2000 < (2A)/D < 5000$	coarse grains
		$1000 < (2A)/D < 5000$	fine grains
Clifton and Dingler (1984)	field and laboratory	$1000 < (2A)/D < 3000$	

grain size (λ_{orb}/D). The ratio of wavelength to grain size of orbital ripples is greater than 100 and less than 2000 (Clifton and Dingler, 1984). Figure 1.2 depicts the raw data, as well as the categorization of Clifton and Dingler (1984) on a plot of normalized wavelength versus normalized wave orbital diameter.

Wiberg and Harris (1994) use a variety of field and laboratory observations to model sedimentary structures in an attempt to easily predict ripple type, wavelength, and height that would be universal for data collected both in the laboratory and in the field. Using small amplitude wave theory, Wiberg and Harris (1994) determine the diameter of orbital motion just above the bed by the equation

$$(2A) = \frac{H}{sinh(kh)} \tag{1.4}$$

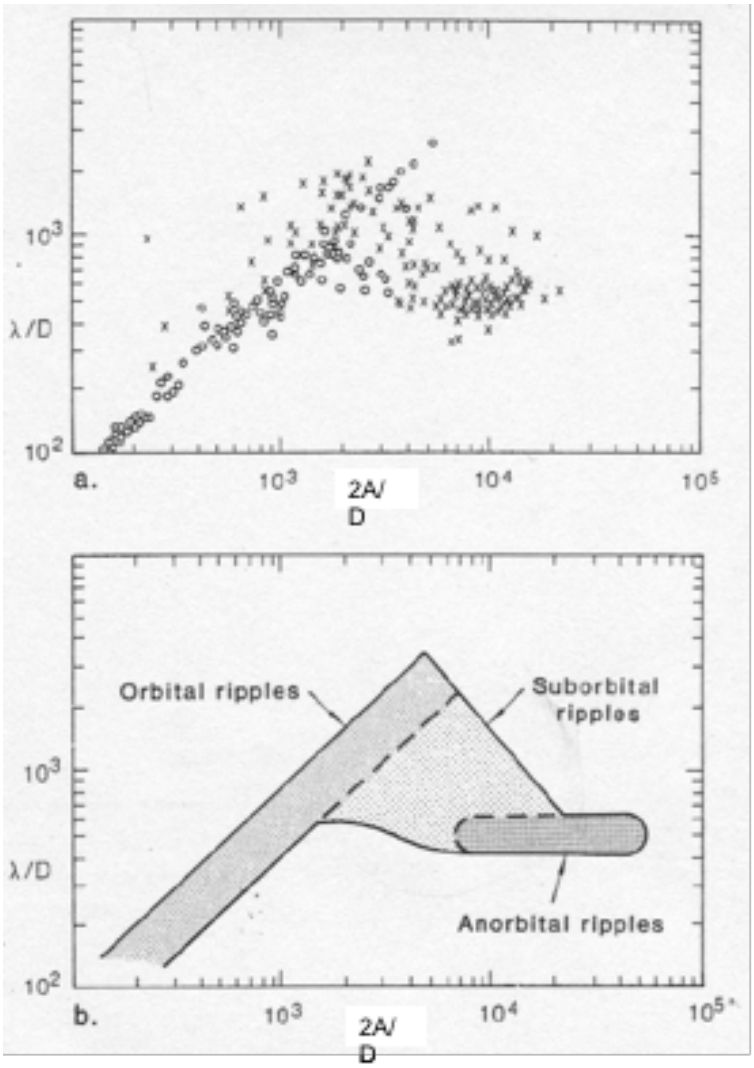

Figure 1.2: Top panel (a) shows ratio of ripple spacing to grain size versus orbital diameter to grain size for both field (crosses) and laboratory (circles) data sets. Bottom panel (b) shows ripple classification scheme. Figure adapted from Clifton and Dingler (1984)

where H is the wave height, h is water depth and k is the wave number, 2π / length of surface gravity wave (L). Data is distinguished between laboratory and field and represented on plots of λ/D vs. $(2A)/D$ and η/D vs $(2A)/D$ (Figure 1.3). Wiberg and Harris (1994) use a large set of combined field and flume data to provide a good characterization of ripple

wavelength and steepness. In an attempt to ensure ripples were in equilibrium, Wiberg and Harris (1994) only included data in which 80% of the critical shear velocity for incipient motion ($0.8u^*_{cr}$) was exceeded. Grain size (D), wave period (T), and either orbital diameter ($2A$) or wave height (H) and water depth (h) are assumed to be known and related by $(2A) = H/sinh(kh)$, where kh can be computed iteratively through the relationship $k_D h = kh * tanh(kh)$, where $k_D = 4\pi^2/(gT^2)$. To predict bedform geometries using this technique, first you must determine the ripple type, then compute ripple dimensions based on ripple type and flow characteristics. Through analyzation of the extensive data set, Wiberg and Harris (1994) determine orbital wavelength by its relationship to wave orbital diameter with the equation:

$$\lambda_{orb} = 0.62(2A) \tag{1.5}$$

This relationship suggests that orbital ripple wavelength is smaller than predicted by Clifton (1976). Wiberg and Harris (1994) also categorize orbital ripples by ripple steepness, defined by the ratio of ripple height over ripple wavelength $(\eta/\lambda)_{orb}$. They determine ripple steepness of orbital ripples to remain nearly constant when $(\eta/\lambda)_{orb} = 0.17$. Figures 1.3 (a) and (c) depict the Wiberg and Harris (1994) normalized ripple wavelength as a function of normalized orbital diameter. Orbital ripple measurements fall along the positively sloped dotted line, representing the relationship: $\lambda_{orb} = 0.62(2A)$. Figures 1.3 (a) and (b) depict data that use symbols to distinguish between laboratory and field data, where as (c) and (d) distinguish data by ripple classification (orbital, anorbital, or suborbital). Figure 1.3 (b) shows the relationship between normalized ripple hight as a function of normalized wave orbital diameter, while (d) represents ripple steepness (η/λ) as a function of orbital

diameter. Wiberg and Harris (1994) determined that orbital ripples have a bedform height which exceeds twice the thickness of the wave boundary layer, or $(2A)/\eta < 12$.

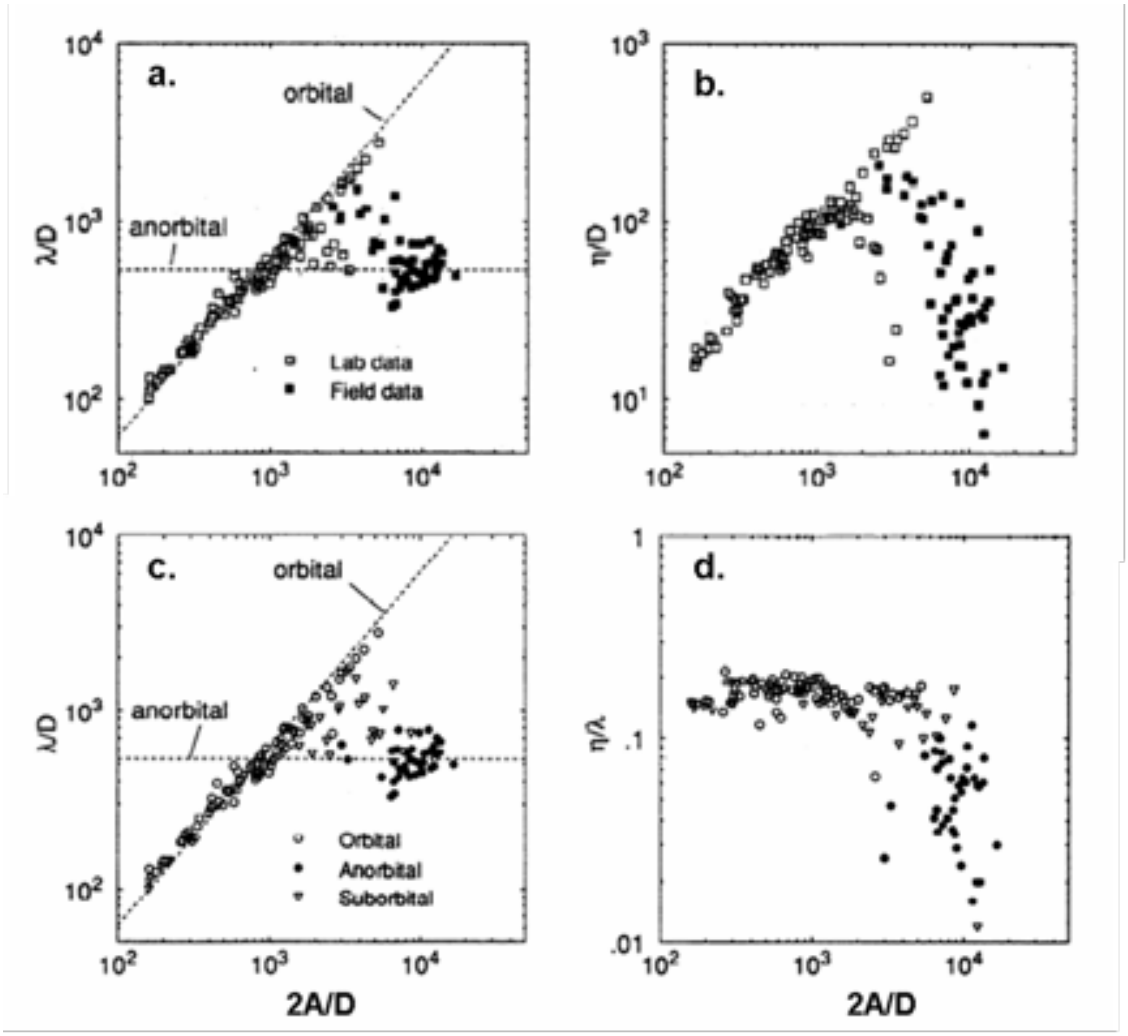

Figure 1.3: Measured (a) ripple wavelength (λ) versus orbital diameter ($2A$) normalized by grain diameter (D). Measured (b) ripple height (η) versus orbital diameter ($2A$) normalized by grain diameter (D). Figures (a) and (b) distinguish between experimental and field data. Measured (c) wavelenth versus orbital diameter and (d) ripple steepness (η/λ) versus orbital diameter normalized by grain diameter and distinguished by ripple classification. Dotted lines in (a) and (c) represent trends in ripple type. Figure adapted from Wiberg and Harris (1994)

Anorbital ripples, the second class of symmetric ripples proposed by Clifton (1976), form as seabed geometry stabilizes under larger values of wave orbital diameter. Anorbital ripples are most commonly found in areas where the bed consists of fine sediment and long wave periods (i.e. $d_{50} = 0.125$ mm, and period = 12 seconds) (Clifton and Dingler, 1984). Similar to the Clifton (1976), Clifton and Dingler (1984) anorbital ripples form when the value of $(2A)/D$ exceeds 5000. The independence of orbital diameter on anorbital ripple geometry results in a wavelength as solely a function of grain size. In Clifton and Dingler (1984), this relationship is $\lambda_{ano} = 400D - 600D$. Wiberg and Harris (1994) suggest that suborbital and anorbital ripples predominantly occur in the field, and are less likely to be found in the laboratory. They also found that anorbital ripples have a maximum steepness smaller than that of orbital ripples, with values near 0.12. Anorbital ripple heights less than one-fourth of the boundary layer height, or $(2A)/\eta > 100$. Smaller ripple heights are associated with anorbital ripples, and are believed to be a result of larger amounts of suspended sediment at ripple crests, due to increased forcing. Although there was a fair amount of scatter, Wiberg and Harris (1994) predicted that $\lambda_{ano} = 535D$ for anorbital ripples. They also found ripple steepness to decrease with increasing flow intensity.

Crawford and Hay (2001) collected field data during an autumn storm event in 1995 on Queensland beach, Nova Scotia, Canada using acoustic scanning sensors and a high-resolution laser-video bed profiling system. Ripple wavelengths were found to be between 8-9 cm and ripple height of 0.2-0.4 cm. Images were collected at 2 Hz and averaged over 40 profiles. Ripple statistics were determined over 8 minute averages. They oserved that, in general, the ripples persist for much longer than a wave period time scale (Crawford and Hay, 2001). As ripple wavelength showed little variability throughout the experiment, an average wavelength of 8.5 cm is used as a constant value in their model. They observed a lack of

dependence of ripple wavelength on wave orbital diameter, suggesting anorbital ripples, and large orbital excursion-to-ripple wavelength ratios (5 to 10) that was consistent with Clifton and Dingler (1984). However, as depicted by Figure 1.4, the anorbital ripple class extends into a smaller normalized orbital diameter range ((2A)/D) than predicted by Clifton and Dingler (1984). These findings were consistent with that of Wiberg and Harris (1994) with a consistent anorbital ripple wavelength of $\lambda_{ano} = 535D$. Anorbital ripple characterization data for all the experiments is presented in Table 1.2.

Suborbital ripples represent the third and final ripple classification under the symmetric bedform sediment transport regime introduced by Clifton (1976). This type of ripple is the most complicated of the three, as its properties are poorly understood and its geometry is an unknown function of both wave orbital diameter ($2A$) and grain size (D). Suborbital ripples are recognized as decreasing in ripple wave length (λ_{sub}) as orbital diameter increases. Clifton and Dingler (1984) determine that the range of the suborbital ripple class is smaller than determined by Clifton (1976). Rather than distinguishing between coarse and fine sediment grain sizes, Clifton and Dingler (1984) couple the two, publishing a common set of values for the suborbital ripple category. They determine the suborbital ripple class to have the relationship: $1000 < (2A)/D < 3000$, subsequently, falling between the limiting factors for orbital and anorbital ripples. The minimum value of 1000 for the relationship of $(2A)/D$ is consistent with fine grain category in the Clifton (1976) model. However, the maximum value of 3000 is significantly less than the value of 5000 predicted by Clifton (1976). No equations have been derived for the suborbital ripple geometry. In fact, some debate the existence of the suborbital ripple class in its entirety. Wiberg and Harris (1994) concluded that only two primary symmetric ripple subcategories exist, namely, orbital and anorbital. They hypothesized suborbital ripples were merely intermediate forms of these two

main ripple types. They suggested that the ratio of wave boundary layer thickness to ripple height, is the paramount indicator in determining between the two main ripple types. Table 1.3 displays the characteristics of suborbital ripples as defined by different references.

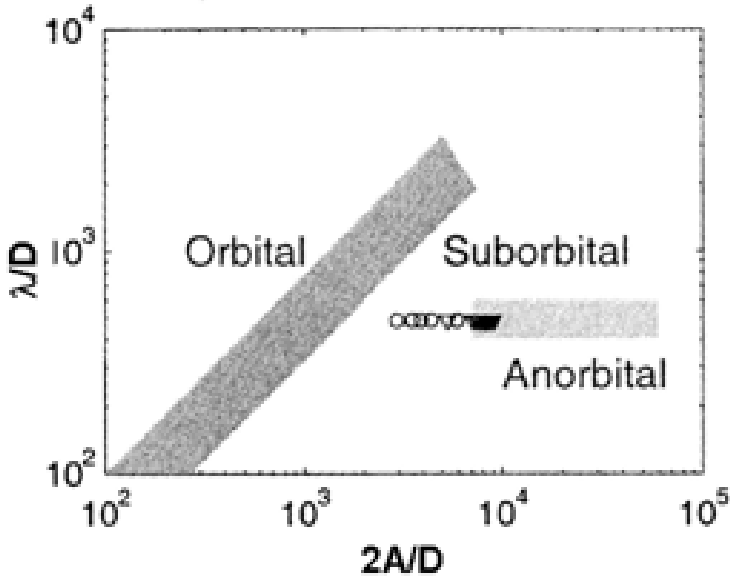

Figure 1.4: Position of Crawford and Hay (2001)'s observed linear transition ripples in normalized wave orbital diameter-ripple wavelength space. Figure adapted from Crawford and Hay (2001)

Hay and Mudge (2005) further investigated bedform response to free surface gravity waves with an extensive data set collected during the Sandy Duck experiment in 1997. Observations were collected at two different locations separated by 40 meters in the cross-shore direction. The mean grain diameter and grain size distributions were nearly identical at these two different locations. The data collection period lasted for 10 consecutive weeks where one dozen storm events took place. The main goal was to determine whether the main factor in determining bed state is related to second-order (e.g. energy) or third-order (skewness or

asymmetry) statistics of the wave field. Sets of 5 acoustic backscatter images of the sea bed, which took 3.7 minutes to collect each set, were averaged every ten minutes during storm intervals, and every thirty minutes during non-storm intervals. Bed state was found to be highly dependant on the root-mean-square wave orbital velocity (u_{rms}), and independent of wave skewness, asymmetry, mean cross-shore current (U), and mean longshore current speed $|V|$. The rms wave orbital velocity is primarily associated with sea-and-swell wave energy. During each of the 12 storm events, Hay and Mudge (2005) observed a common

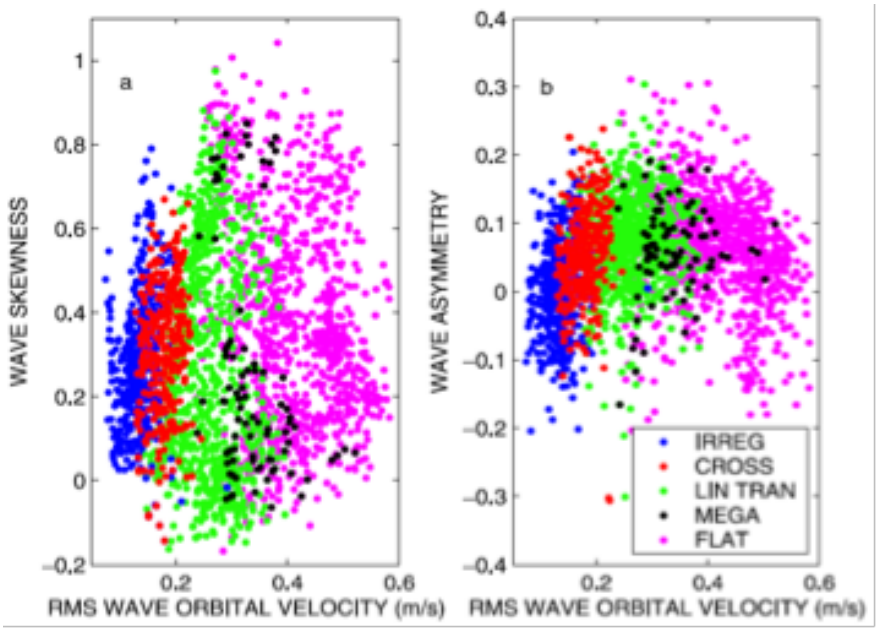

Figure 1.5: Bed state occurrence as a function of root-mean-square wave orbital velocity for wave skewness (a) and wave asymmetry (b). Adapted from Hay and Mudge (2005)

bed state evolution when the sea started calm until the height of the storm. They witnessed irregular ripples under relatively mild wave conditions, which progressed to cross ripples, then to linear transition ripples and finally a flat bed resulted with high wave energies. This same progression followed in reverse as the storm calmed, revealing a definite evolution of

the sea bed geometry throughout each of the storm events. This repetition of bed states reveals a lack of dependence on previous bed state as the bed adjusts to changes in the wave forcing.

Due to the nearly identical grain size distribution parameters at the two frames, grain size (D) was omitted as a contributor to bed state variability observed at the two stations. Period (T) was also able to be eliminated because there was negligible difference in peak period between the five different bed states considered. Further simplifications were made as experimental mean u_{rms} values were similar at the two data collection stations. Through careful analysis, Hay and Mudge (2005) determined that for the Sandy Duck 97 data set, wave nonlinearity does not indicate bed characteristics and therefore should not be included in any predictive models. Furthermore, rms wave orbital velocity is the critical parameter for determining bed state.

Further examination of the Clifton (1976) conceptual model were completed by Brown (2006). Data was collected during the CROss Shore Sediment Transport EXperiment (CROSS-TEX), at the O. H. Hinsdale large scale wave flume at Oregon State University. Images of the sea bed were collected using a submerged Particle Image Velocimitry laser-video system. Ripple geometry measurements were manually estimated with the bedform images. Bed states were found to range from rippled to flat. Based on the lack of dependence of ripple wave length to wave orbital diameter, bedforms observed at both water depths investigated were determined to be anorbital. According to the ripple classification scheme of Clifton and Dingler (1984), Brown (2006) found that the anorbital ripple type extends into a smaller range of wave orbital diameters than determined by Clifton and Dingler (1984), consistent with the findings of Crawford and Hay (2001). Consistent with Hay and Mudge (2005), u_{rms} was found to be the most useful measurement for classifying ripples and predicting flat bed.

CHAPTER 2

OBSERVATIONS

Observations were obtained at the O. H. Hinsdale Wave Research Laboratory large scale wave flume at Oregon State University in 2005. The goal of the collaborative CROss Shore Sediment Transport EXperiment (CROSSTEX) was to achieve a greater understanding of near shore dynamics, including: sediment transport, boundary layer characteristics, ripple formation, bed state variability and transformation, and vortex ejection. This specific investigation focuses on bed state variability and bed state evolution influenced by free surface gravity waves. The wave tank is 110 m long, 3.7 m wide, and 4.6 m deep. Waves are generated by a hydraulically driven, hinge-type wave paddle. The paddle is capable of generating oscillatory flow with field-scale regular and irregular wave conditions. Observations were obtained under random wave conditions using a TMA spectrum with significant wave heights (H_{mo}) ranging from 30 to 60 cm and wave periods (T) in the range of 4 to 8 seconds. The relatively narrow tank allows a negligible cross-shore current typically found in nature, simplifying the collected data. Wave runs were generally shorter than 20 minutes to reduce tank seiche. The coarse grained sediment that filled the flume had a median grain diameter (D) of 0.0218 cm.

2.1 Instrumentation

Observational instrumentation was deployed from a single mast, fixed to a cart resting on the tank side walls. The cart was moved to two different locations in the along-tank direction during the experiment. Station 1 is located 40 meters offshore in a water depth of 1.723 m. Station 2 is located 30 meters offshore in a water depth of 1.625 m. Both Station 1 and Station 2 are located offshore of the wave breaking region.

Three components of free stream velocity are collected with an Acoustic Doppler Velocimeter (ADV) located approximately 30 cm above the bed. The ADV collected velocity measurements continuously for the entire duration of each run at a sample rate of 25 Hz. A pencil beam, two axis rotating sonar, also mounted to the mast, collects larger scale bedstate characteristics such as local beach slope.

Flow field and seabed geometry data were collected using a submersible Particle Image Velocimetry (PIV) system. The Dantec PIV system consists of a variable power 120 mJ Nd:Yag laser and a 1.0 megapixel digital camera. An optical lens at the laser head transforms the laser beam into a laser sheet with adjustable thickness. The laser sheet is oriented in the x-z plane, allowing for the measurement of onshore/offshore (u) velocities as well as vertical velocities. A diagram of the complete instrument setup is depicted in Figure 2.1. The camera field of view was roughly 23 cm x 23 cm. Cross-shore (y) velocities are negligible due to the narrowness of the flume and lack of cross-shore current in the flume. Both the laser and the camera components of the PIV system are mounted in water tight housing for their underwater deployment. The underwater camera housing was mounted to the side wall of the tank at a slightly downward looking angle. The oblique camera angle was instituted to avoid foreground ripples from shadowing laser reflection near the bed in the images at the area of interest. Images were collected at a rate of 15 Hz and stored in a remote buffer. Due to

system limitations, 48 seconds of data (720 images) are collected successively and temporarily stored in the system buffer. Upon completion of collection, the buffer downloads the 720 collected images to a local computer hard drive via ethernet connection. Buffer downloads result in gaps of time between successive PIV data collection sessions. Figure 2.2 shows a sample 8 minute window with five 48-second windows of PIV observations.

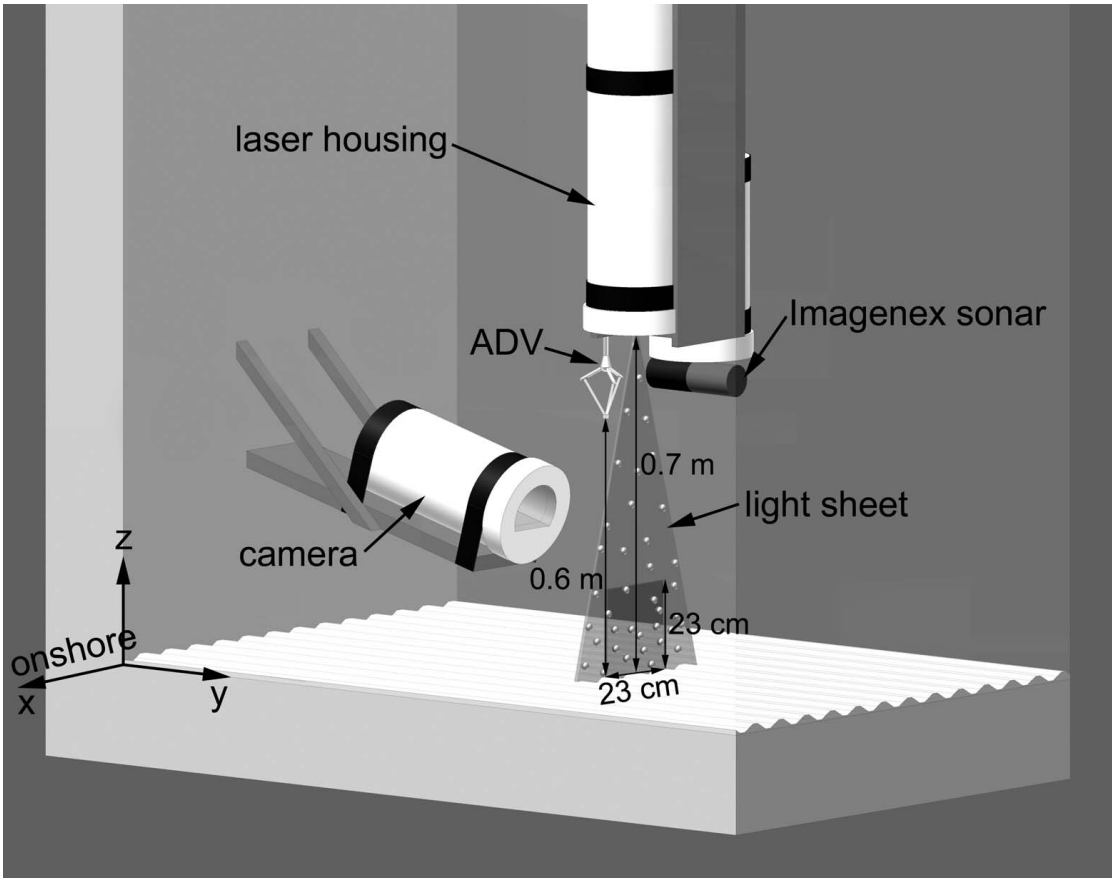

Figure 2.1: Instrument setup at CROSSTEX. Figure adapted from Nichols and Foster (2007)

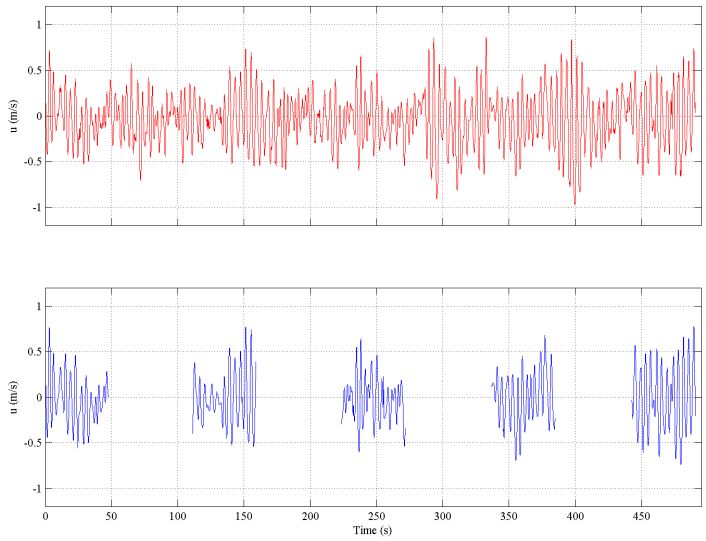

Figure 2.2: Velocity measurements explain the lapse in time between PIV data recordings. Top figure depicts onshore (u) velocity versus time as measured by the Acoustic Doppler Velocimeter in red. Bottom figure shows u velocity versus time as measured by the Particle Image Velocimetry system in Blue. The discontinuity in the bottom diagram represents time when buffer downloads images to computer hard drive, resulting in interrupted PIV data.

2.2 Ripple Geometry Measurements

Observed bed geometries range from rippled to flat. The two-dimensional sea bed profile over 23 cm is large enough to observe multiple wavelengths in each image, and detailed enough to observe slight alterations in ripple characteristics, such as the radius of curvature and ripple height. Following the method of Nichols and Foster (2007), the bed is determined by the intensity of the light reflected by the sediment bed. Due to the suspension of sediment and other debris in the water column, consecutive images are averaged by their pixel intensity. In the case of this study, images have been averaged over both 8 and 48 second windows. For 8 second averages, 120 consecutive images are averaged, with a 50% overlap between

consecutive average images. 48 second averages simply determine the mean pixel values for an entire setup of 720 images (48 seconds of data). In this algorithm, the highest pixel intensity range is defined to be within 5% of the maximum pixel intensity in each vertical column. Thus, an upper and lower bound for the corresponding range is determined in each column. The centroid of this area is defined as the bed profile. Figure 2.3 shows two examples of how the bed profile is calculated. The solid green line traces the sea bed profile. The maximum pixel intensity range is outlined by the green dashed line on either side of the bed profile. Figure 2.3a shows an example of flat bed, whereas 2.3b reveals a rippled bed state.

Ripple height is the vertical distance measurement from the trough of one ripple to the crest of an adjacent ripple. Following Crawford and Hay (2001), bedforms are assumed to be roughly sinusoidal and ripple height (η_{std}), is calculated as $2\sqrt{2}$ multiplied by the standard deviation of the bed profile.

Following Nichols and Foster (2007), radius of curvature (herein RC) is used in this investigation to quantify the curvature of the bedform crests and troughs. RC characterizes the radius of a circle that matches the roundness of a curve. Figure 2.4 explains the idea of RC and gives an example of what the RC looks like when fit in a theoretical curve. As made obvious by this figure, a larger RC is associated with a more gentle curve, while a smaller RC is associated with a sharper curve.

Ripple wavelength (λ_b) is determined as the distance between adjacent ripple crests or the distance between adjacent ripple troughs. The crest and trough are identified as the local maxima and minima in the bedform profile, respectively. Multiple wavelengths of the ripples are obtained for each profile. Ripple wavelength does not make the same characterization of ripple geometry as ripple height or RC of the crest and trough. The three previous

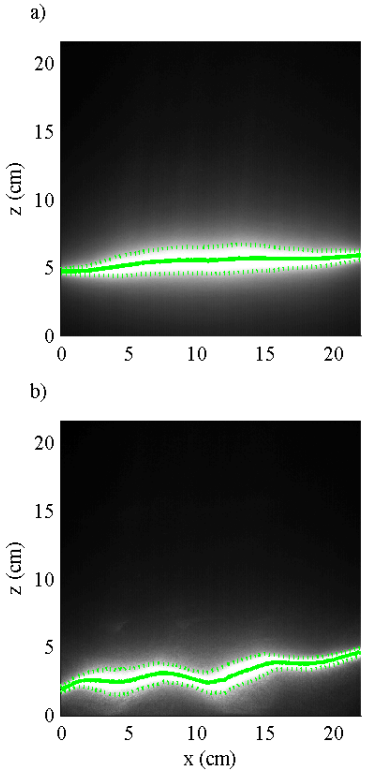

Figure 2.3: Calculation of sea bed profile. The solid green line traces the sea bed profile. The 5% maximum pixel intensity range is outlined by the green dashed line on either side of the bed profile. Figure 2.3a and b show an example of flat and rippled bed states, respectively.

characterizations of ripple geometry predict the ripple geometry and steepnesss. Conversely, ripple wavelength does not do as well of a job characterizing the ripple shape. For this reason, bed form wave length will not be discussed or analyzed at length; however, the average wave length over the entire wave simulation will be given for each wave simulation under consideration.

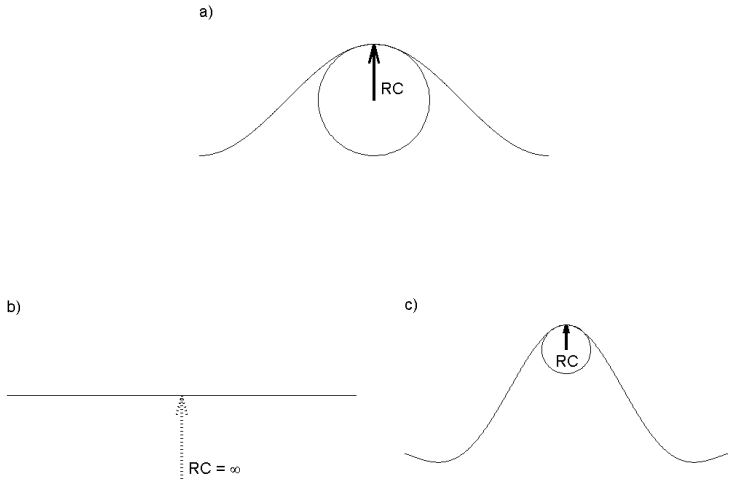

Figure 2.4: RC examples for a) gentile crested ripple, b) flat, and c) sharp crested ripple. Figure adapted from Nichols and Foster (2007)

CHAPTER 3

RESULTS

3.1 Bed State Variability

Sea bed geometry characteristics were found to change considerably over relatively short temporal scales in some instances and not in others. On the contrary, the geometry characteristics remained nearly static over a greater time scale. In order to characterize this evolution, the bed was examined over two different averaging increments. Images were averaged over 8 second intervals with a 50% overlap to ensure geometry transformations over short temporal scales were identified and examined. Forty-eight second average bedform characteristics were also investigated to study variations in sea bed geometry over longer temporal scales.

Figure 3.1 shows an example of the wave and bed geometry variability over a 7.3 minute wave simulation. Five sets of PIV observations were collected over the 7.3 minutes. A 40 cm significant wave height and a peak period of 8 seconds with a TMA spectrum resulted in root-mean-square velocities ranging from 20 to 40 cm/sec (Figure 3.1b). Figure 3.1c shows the 48 second bed profile and its temporal evolution. The bed is originally quite rippled with distinct crests and troughs. The third bed profile, at 210 seconds, shows a much flatter bedform profile with gentler flatter ripple crests. As simulation progresses, the final

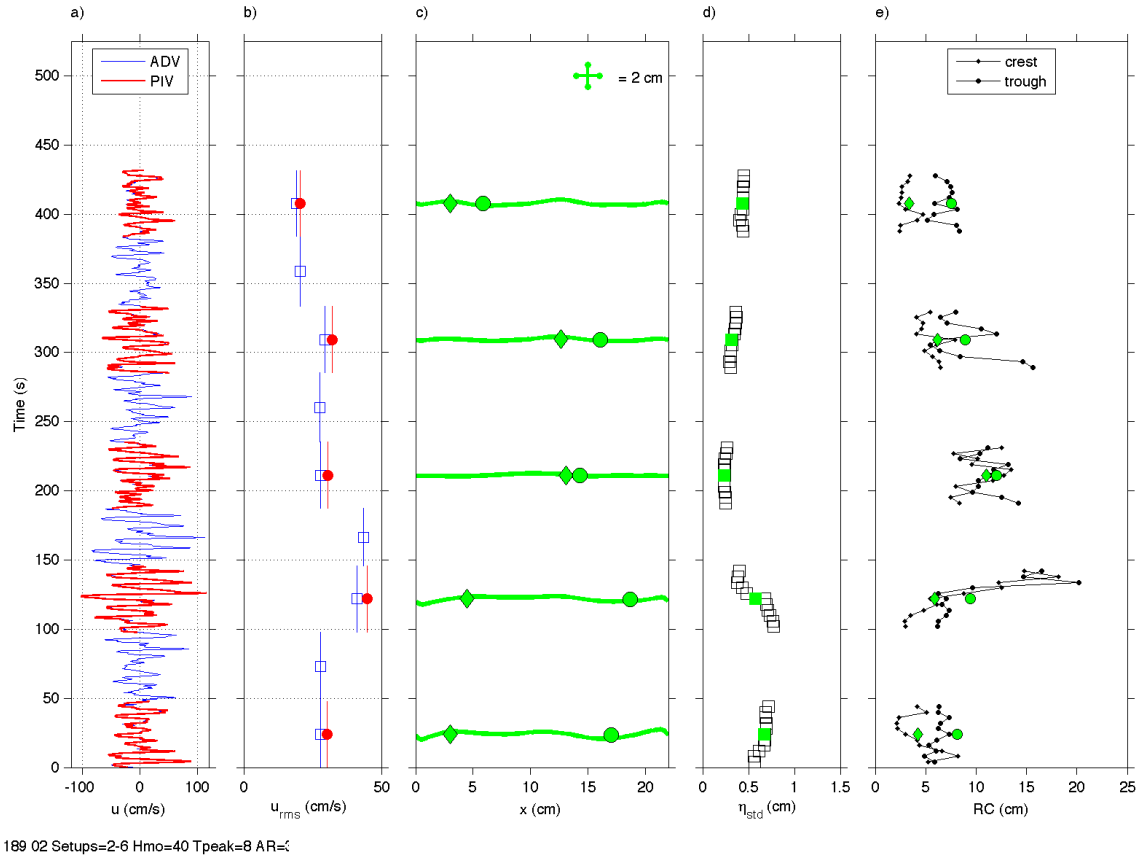

Figure 3.1: Velocity and sea bed geometry resulting from 40 cm significant wave height and 8 second peak period. a) Velocity data as collected by the PIV system (red) and ADV (blue). b) Root-mean-square velocity over 48 second time intervals, using the same color scheme as a). 48 second average bedforms are depicted in c). Diamond and circular markers on each bedform reveal the location of the crest and trough locations used for *RC* measurements. d) Ripple height for 8 (black) and 48 (green) second average bedforms. e) *RC* measurements for 8 (black) and 48 (green) second average bedforms.

48 second average bedform more closely resembles the initial bedform by becoming more rippled and showing distinct ripple crests. Ripple heights are initially just over 0.5 cm at the commencement of the run data collection. A distinct and rapid decrease in ripple height is evident over the second PIV observation window. During this 48 second time period, ripple height decreases from 0.6 cm to 0.3 cm. Over the next three sets of PIV observations

recorded in the 5 minutes following, ripple height steadily increased to 0.5 cm. Figure 3.1e shows the crest and trough radius of curvature. With peaky crests and flatter troughs, crest RC is always a lesser value than the trough RC. Initially, the RC is consistently less than 5 and 10 cm for the crest and trough, respectively. In the second PIV observation set, the RC increases rapidly to values greater than 20 cm. The swift increase in RC is suggestive of a flat bed and is coincident with the rapid decrease in ripple height. Following the bed flattening, the RC stays consistent at around 12 cm and then decreases until the end of the 5th PIV observation where RC measurements return to their initial values of less than 5 and 10 cm for the crest and trough. The flattening of the bed in the second and third PIV observations is consistent with a large root-mean-square velocity of just under 0.5 m/sec. Notice that over the relatively short duration of a wave run, geometry characteristics show considerable variability.

Figure 3.2 shows an example of the wave and bed geometry variability over the 7.3 minute wave simulation of Figure 3.1. Five sets of PIV observations were collected over the 7.3 minutes. A 40 cm significant wave height and a peak period of 8 seconds with a TMA spectrum resulted in a root-mean-square velocity of 30 cm/sec. As Figure 3.2a shows, the root-mean-square velocity over individual 8 and 48 second averages varied from 12 to 60 cm/sec and 20 to 45 cm/sec, respectively. An average wavelength of 7 cm was observed over the run. The ripple height indicators of RC_{crest}, RC_{trough}, and η_{std} show a considerable amount of scatter. Figure 3.2b shows the bedform ripple height over individual 8 and 48 second averages ranging from 0.25 to 0.75 cm and 0.25 to 0.65 cm, respectively. Figure 3.2c shows a considerable amount of variability in RC_{crest}, ranging from 2 to 15 cm and 3.5 to 12 cm for their respective 8 and 48 second averages. Likewise, RC_{trough} observations shown in figure 3.2d reveals considerable scatter with 8 and 48 second individual bedform

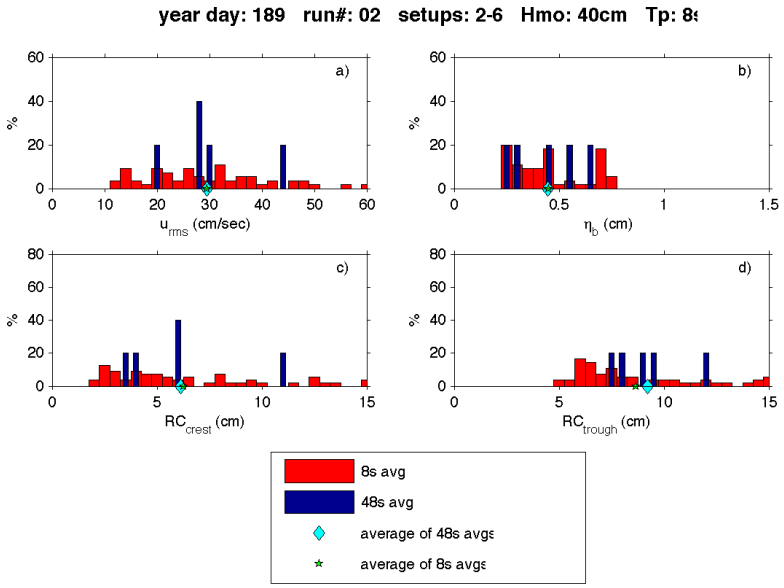

Figure 3.2: Histogram of ripple geometry characteristics and root-mean-square velocity. Red bars represent the histogram of the 8 second average bedform profile characteristics. Blue bars are representative of the 48 second average bedform characteristics. The star and diamond symbols mark the location of the arithmetic mean of all the individual 8 and 48 second average bedform data, respectively.

averages ranging from 5 to 15 cm and 7.5 to 12 cm respectively. Although the individual measurements of wave and bedform characteristics show much variability, the overall average value of the individual observations for the 8 and 48 second averages prove to be remarkably consistent.

Figure 3.3 shows an example of the wave and bed geometry variability over a 7 minute wave simulation. Five sets of PIV observations were collected over the 7 minutes. A 30 cm significant wave height and a peak period of 4 seconds with a TMA spectrum resulted in root-mean-square velocities (u_{rms}) ranging from 10 to 20 cm/sec (Figure 3.3b). Figure 3.3c shows the 48 second bed profile and its temporal evolution. Throughout the 7 minute

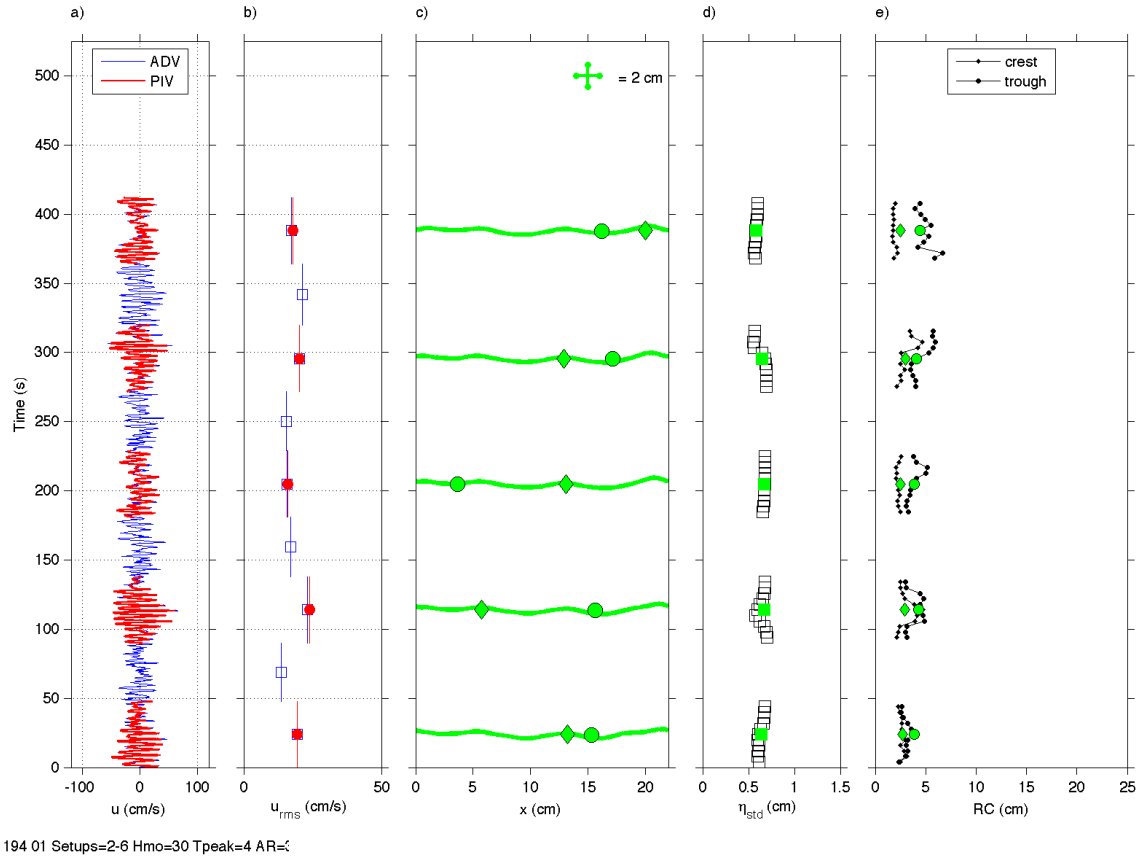

Figure 3.3: Velocity and sea bed geometry resulting from 40 cm significant wave height and 8 second peak period. a) Velocity data as collected by the PIV system (red) and ADV (blue). b) Root-mean-square velocity over 48 second time intervals, using the same color scheme as a). 48 second average bedforms are depicted in c). Diamond and circular markers on each bedform reveal the location of the crest and trough locations used for RC measurements. d) Ripple height for 8 (black) and 48 (green) second average bedforms. e) RC measurements for 8 (black) and 48 (green) second average bedforms.

collection duration, the bed profile changes very little. The bed is quite rippled and crests are easily identified. There is low variability of the ripple shape in each of the 48 second bedform averages (Figure 3.3c). The consistency in bedform shape is also consistent with the ripple height of a nearly constant value of just over 0.5 cm (Figure 3.3d). Similarly, RC data shown in Figure 3.3e changes very little throughout the wave simulation. RC_{crest} and

RC_{trough} are initially less than 4 cm, and only a slight increase in RC_{trough} is observed in the final two PIV recording sets, yielding maximum RC values of 6 cm.

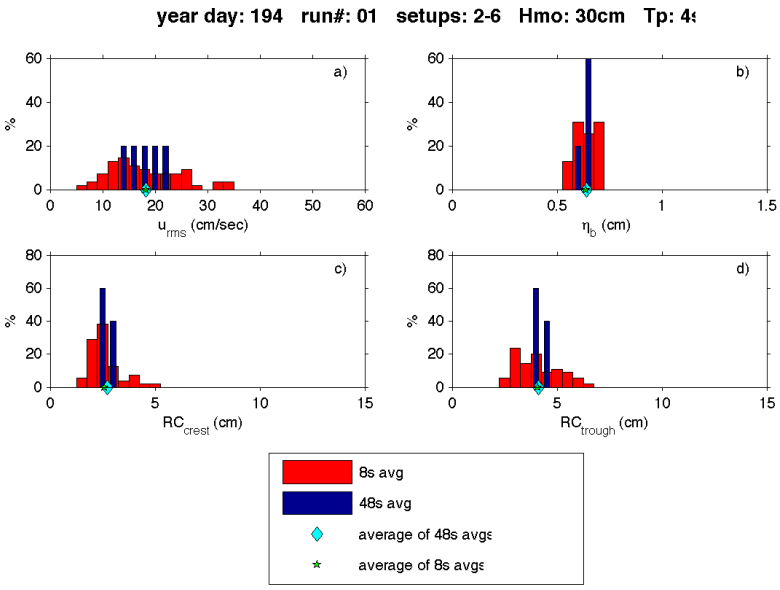

Figure 3.4: Histogram of ripple geometry characteristics and root-mean-square velocity. Red bars represent the histogram of the 8 second average bedform profile characteristics. Blue bars are representative of the 48 second average bedform characteristics. The diamond symbol marks the location of the arithmetic mean of all the 48 second average bedform data. The star depicts the location of the mean of all 8 second average bedform data for the run.

Figure 3.4 shows an example of the wave and bed geometry variability over the same 7 minute wave simulation of Figure 3.3. Five sets of PIV observations were collected over the 7 minute duration. A 30 cm significant wave height and a peak period of 4 seconds resulted in an overall root-mean-square velocity of 18 cm/sec. Figure 3.4a shows that u_{rms} over individual 8 and 48 second averages varied from 5 to 35 cm/sec and 12 to 22 cm/sec respectively. This histogram data reveals a relatively consistent values for root-mean-square

velocity over the duration of this particular run for individual 8 second averages. Similarly, individual 48 second root-mean-square velocities reveal a normal distribution. Far less variability in ripple geometry characteristics is observed corresponding to these particular wave conditions. 3.4b shows the bedform ripple height over individual 8 and 48 second average bedforms ranging from 0.55 to 0.75 cm, respectively. Crest RC data ranged from 2 to 5 cm for individual 8 second bedform averages, while 48 second average bedforms consistently yielded RC_{crest} measurements of 2.5 cm as can be seen in figure 3.4c. Figure 3.4d shows the RC_{trough} for individual 8 and 48 second averages ranged from 2.5 to 7 cm and 4 to 4.5 cm, respectively. Average ripple wavelength over the run was 7 cm. Overall averages of individual 8 and 48 second bedform geometry characteristics were consistent for each of the ripple height indicators investigated. Figure 3.4 shows a relatively normal distribution of values for each of the characteristics measured with little scatter and low variability in the data.

Histograms of wave and bed data also reveal the consistency between 8 and 48 second averaging times. Vertical blue bars representing individual 48 second averages in figure 3.5 closely resemble the data trends of 8 second individual averages, depicted by the red vertical bars. Figure 3.5a shows u_{rms} velocity data ranging from 10 to 38 cm/sec and 18 to 24 cm/sec for individual 8 and 48 second averaging times. Although the 8 second data contains a considerably larger amount of variability, the most frequent velocities observed (distinguished by the highest red bars) occur in the same bins ranges of the 48 second averages. This trend is also revealed in the bed geometry histogram data in Figures 3.5b, c, and d. The 48 second average bedform data matches up well with the most frequently observed 8 second data. Figure 3.5b shows a peak in the most common ripple height measured at 0.6 cm, which also corresponds to the most frequently observed 48 second ripple height.

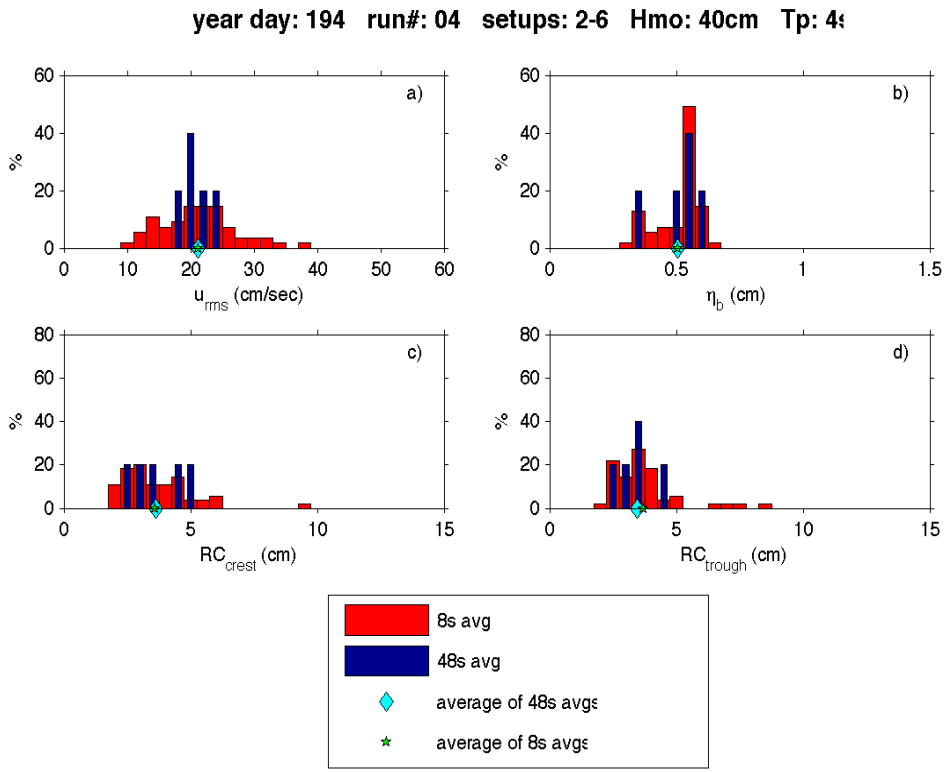

Figure 3.5: Histogram of ripple geometry characteristics and root-mean-square velocity. Red bars represent the histogram of the 8 second average bedform profile characteristics. Blue bars are representative of the 48 second average bedform characteristics. The diamond symbol marks the location of the arithmetic mean of all the 48 second average bedform data. The star depicts the location of the mean of all 8 second average bedform data for the run.

Figure 3.6 shows variability in velocity and ripple geometry for 12 different wave simulations. Similar to Figure 3.5, Figure 3.6 shows reasonable uniformity between 8 and 48 second average data. These figures show consistency between 8 and 48 second average bedform data for root-mean-square velocity, ripple height, and trough radius of curvature. For these particular data sets, 48 second average bedform data is representative of the entire data set, thus deeming the 8 second bedform averages unnecessary.

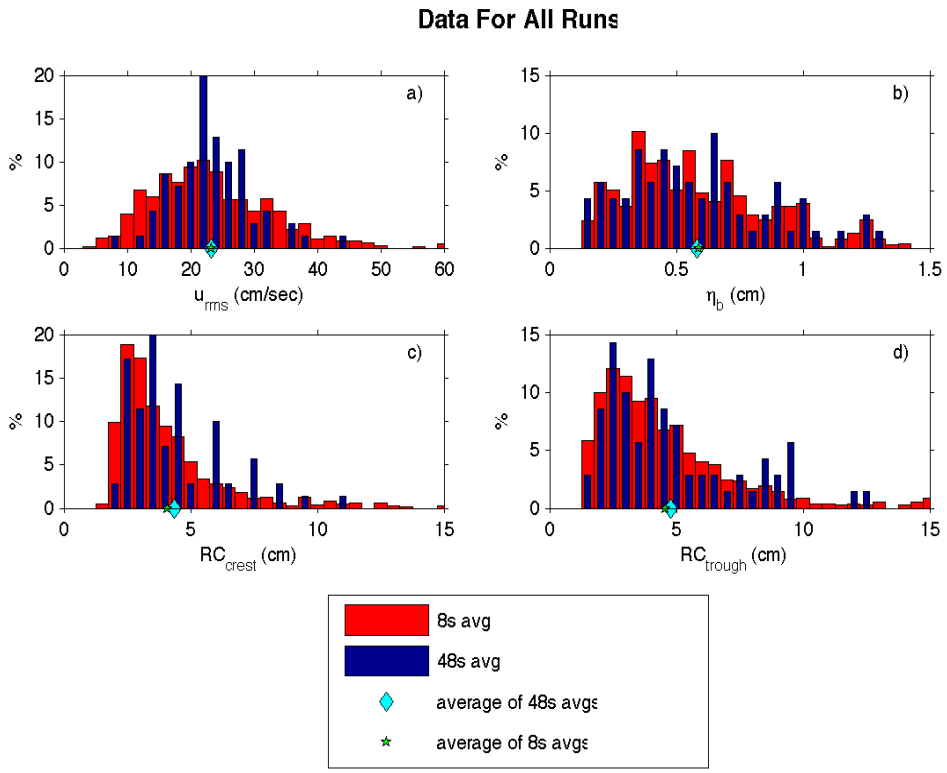

Figure 3.6: Histogram featuring all bedform data collected during twelve runs at CROSSTEX. Red and blue bars represent 8 second and 48 second average bedform data, respectively. Diamond and star represent the average of all 48 second and 8 second bedform data.

However, 48 second bedform data is not representative of all 8 second average bedform characteristics during a given wave simulation. Figures 3.2 and 3.7 show large variations between 8 and 48 second averages, most notably in the root-mean-square velocity and RC data. Peaks in 8 second data observed in these figures often do not correspond to a peak in 48 second data. Figure 3.7c supports this claim. The majority of the RC_{crest} 8 second average observations occurred in the 2 to 4 cm range, however, peaks in 48 second average data are shown to be as high as 8.5 cm. This inconsistency is also depicted in Figure 3.7d.

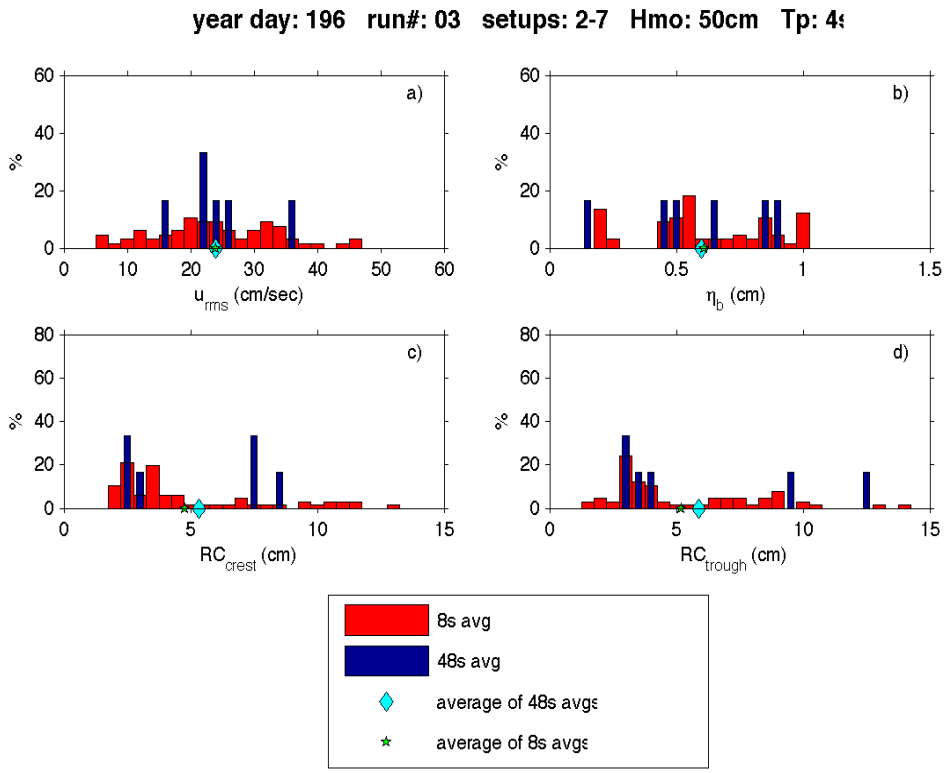

Figure 3.7: Histogram of ripple geometry characteristics and root-mean-square velocity. Red bars represent the histogram of the 8 second average bedform profile characteristics. Blue bars are representative of the 48 second average bedform characteristics. The diamond symbol marks the location of the arithmetic mean of all the 48 second average bedform data. The star depicts the location of the mean of all 8 second average bedform data for the run.

Here, although some of the most commonly observed RC_{trough} data between 8 and 48 second average data are consistent, two occurrences of 48 second average data correspond to a value where no 8 second averaged data was observed. These values are at 9.5 and 12.5 cm. Another example of this inconsistency is shown in Figure 3.2c. A 48 second average RC_{crest} value of 11 cm which makes up 20% of the 48 second data in the category corresponds to 0% of the 8 second average observations.

Notice that the averages of the 48 second data and the 8 second data for each of the bed state characteristics, depicted by the blue diamond and the green star, respectively, are consistently very close to each other on the histograms. This shows that although there is often a considerable amount of variability in the bed state, the long term average of the bed characteristics remains relatively uniform. This overall accuracy of long term data is revealed by the compilation of all histogram data plotted on a single chart for each variable. Figure 3.6 shows that over long periods of time, 48 second average data is a good representative sample of the seabed geometry. Although there is a considerable range in values in each of the characteristics represented, the 48 second averaging time closely resembles the 8 second average bedform characteristics for ripple height and RC_{trough}. Figure 3.6 also depicts the accuracy in not only the shape of the data for each averaging time, but also the over all average of the data represented by the symbols along the horizontal axis for ripple height and RC_{trough}. On the contrary, RC_{crest} observations do not show the same relationship between 8 and 48 second average data. Peaks in the 8 second average RC_{crest} data do not correspond with the peak of the 48 second average data (Figure 3.6c). Forty-eight second average data has a similar shape to 8 second average data, however 48 second values lie to the right of 8 second average values. With RC_{crest} values increasing to the right, this shows that gentler crests were observed for 48 second average bedforms, while peakier crests were observed over an 8 second averaging window. The average of individual 8 and 48 second averages for RC_{crest} supports this claim, revealing a larger value for the average of individual 48 second average bedform data. This demonstrates that over long time periods, 48 second data for η_{std} and RC_{trough} shows a representative sample of the bed state characteristics, while 48 second RC_{crest} data does not. Additional histogram figures are located in the appendix.

However, the long term average is not necessarily representative of all physical processes. Nichols and Foster (2007) found that the ripple steepness and bedform RC directly influence the formation and ejection of vortical structures which in turn suspend sediment into the water column. The smaller the RC (i.e. peakier crests), the more likely it is to form a vortex due to the oscillatory flow of a large body of water.

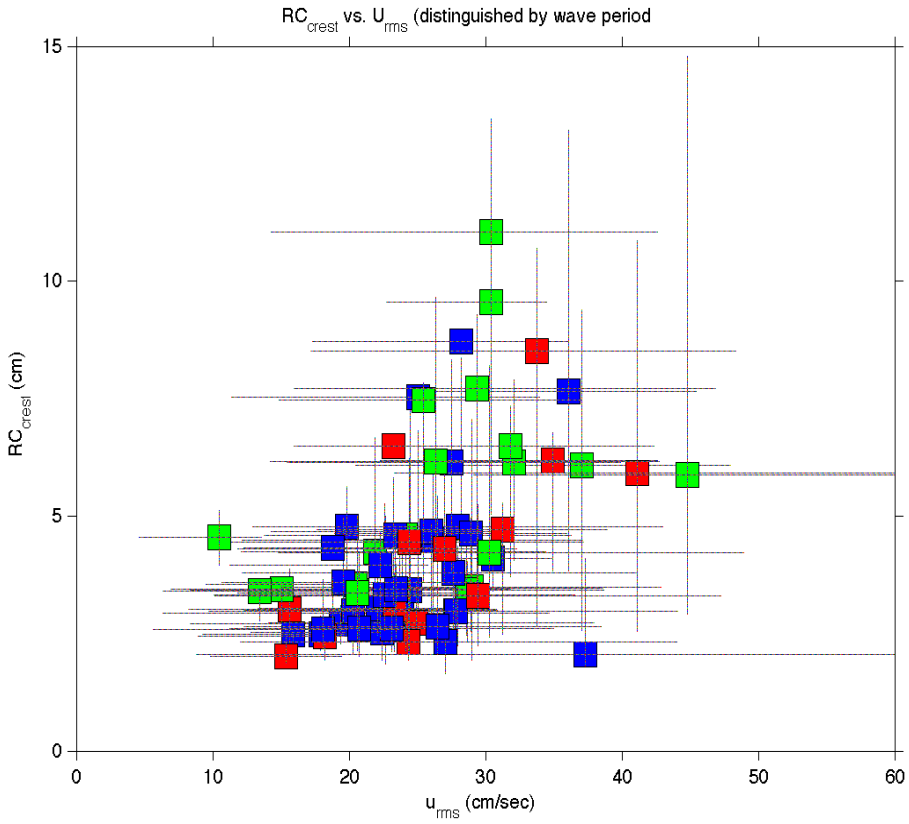

Figure 3.8: RC_c vs. u_{rms}. Blue, red, and green symbols correspond to observations collected with a peak wave period of 4, 6, and 8 seconds, respectively. Marker represents 48 second bedform averages. Lines extend from 8 second average minimum to 8 second maximum values.

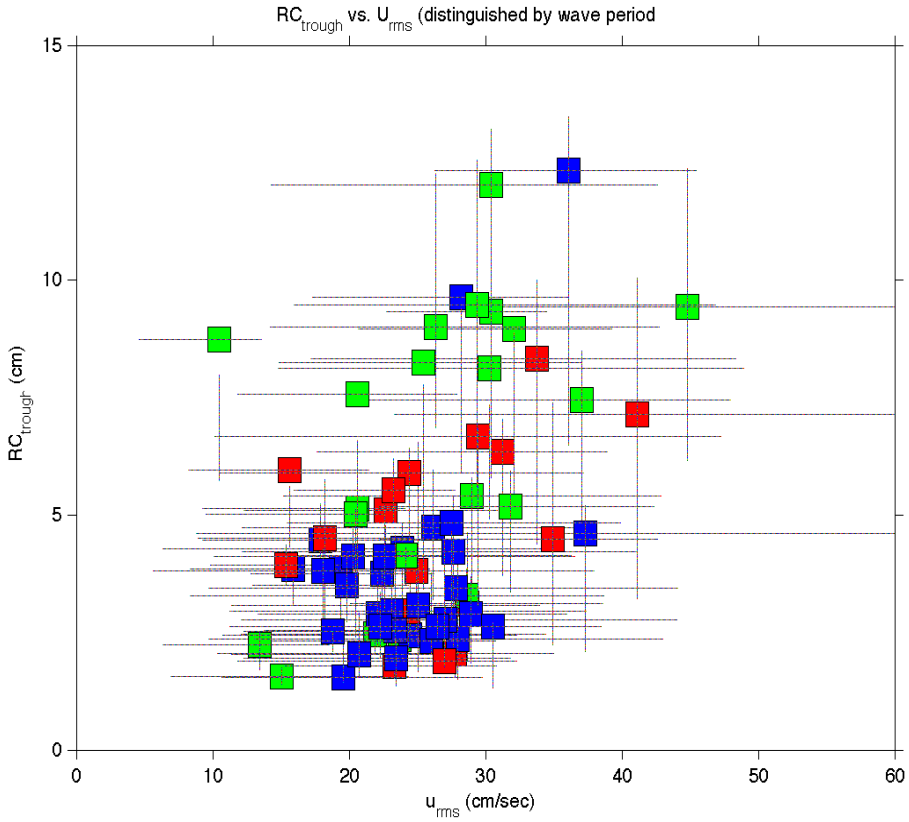

Figure 3.9: RC_t vs. u_{rms}. Blue, red, and green symbols correspond to observations collected with a peak wave period of 4, 6, and 8 seconds, respectively. Marker represents 48 second bedform averages. Lines extend from 8 second average minimum to 8 second maximum values.

It has been proved that seabed profiles change over time, often revealing large amounts of variability in their bed geometry characteristics. Factors that influence the resulting changes in geometry will be examined over the complete data set comprised of 12 data runs. First the effects of root-mean-square velocity on geometry characteristics is investigated. Figures 3.8 and 3.9 show RC data for the crest and trough, respectively, versus u_{rms} velocity. The plotted data represent a trend between these characteristics illustrating that the RC increases with increasing root-mean-square velocity. The random distribution of colors in these figures show

that there is no trend between period and RC. Therefore, it can be concluded that period has no significant effect on RC. Ripple height is plotted versus root-mean-square velocity in Figure 3.10. For larger periods (6 and 8 seconds), Figure 3.10 illustrates an inverse relationship between η_{std} and u_{rms}, which reveals that as u_{rms} increases, η_{std} decreases. However, for smaller (4 second) peak periods, ripple height is independent of u_{rms}. Thus, it can be concluded that period does have an effect on ripple height.

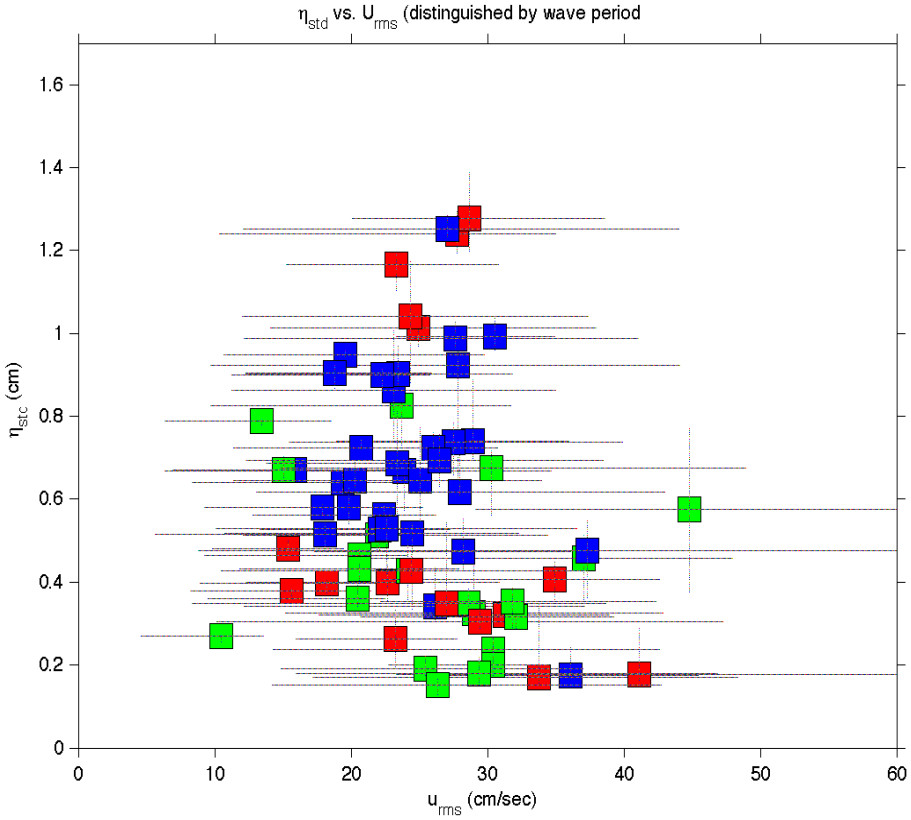

Figure 3.10: η_{std} vs. u_{rms}. Blue, red, and green symbols correspond to observations collected with a peak wave period of 4, 6, and 8 seconds, respectively. Marker represents 48 second bedform averages. Lines extend from 8 second average minimum to 8 second maximum values.

Ripple geometry characteristics were also plotted against root-mean-square velocities; however, this time, the data is distinguished by the significant wave height (H_{mo}). Figures 3.11 and 3.12 show RC data versus u_{rms} with marker colors distinguishing between the wave heights that created the bedforms. For similar values of root-mean-square velocity, RC is relatively larger under conditions of larger wave heights. Fifty cm H_{mo} (green) markers in Figures 3.11 and 3.12 lie significantly higher in the figure than measurements taken under other smaller wave heights. Trends in RC data show that the larger the significant wave height the larger the RC. This means that as the wave height increases, the bed flattens out, as determined by the increasing RC.

No significant trends were observed in respect to ripple height (η_{std}) when distinguished by significant wave height. This is revealed by the random distribution of colors in Figure 3.13. Thus, it can be concluded that significant wave height has no effect on ripple height.

No significant claims can be made about ripple wavelength from the figure featuring ripple wavelength versus root-mean-square velocity. This statement holds true for both figure that is distinguished by wave period and significant wave height. Figures A.18, A.19, and A.20 depict these relationships and can be found the appendix.

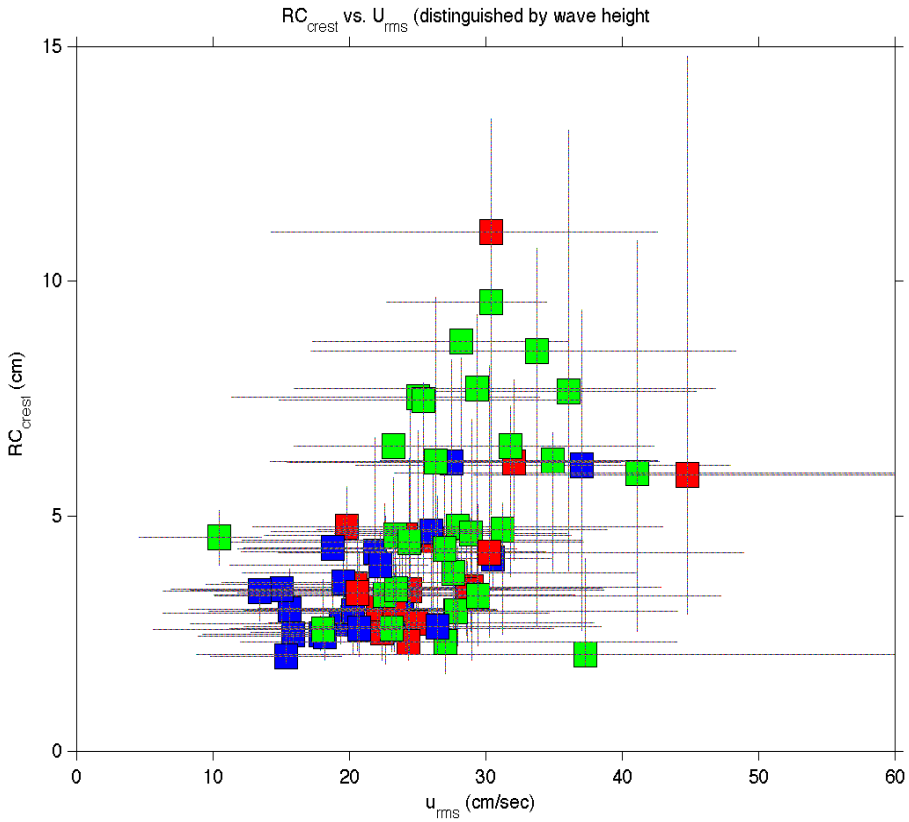

Figure 3.11: RC_c vs. u_{rms}. Blue, red, and green symbols correspond to observations collected with a significant wave height 30, 40, and 50 cm, respectively. Markers represent 48 second bedform averages. Lines projecting from marker represent variability, extending from 8 second average minimum to 8 second maximum values over the 48 second time period.

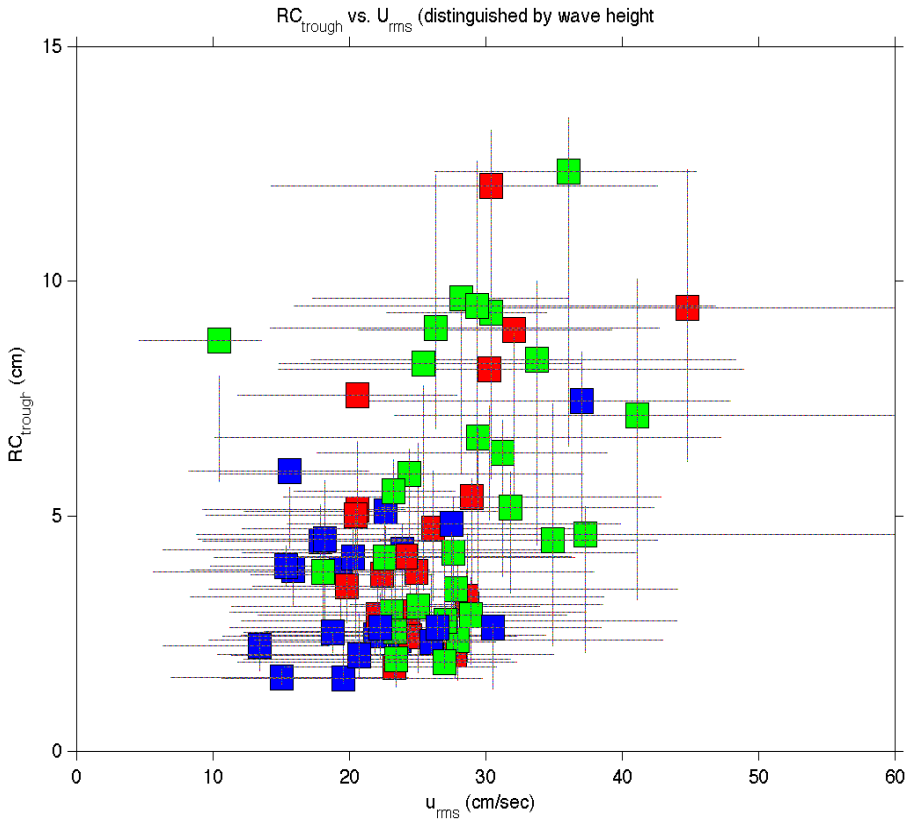

Figure 3.12: RC_t vs. u_{rms}. Blue, red, and green symbols correspond to observations collected with a significant wave height 30, 40, and 50 cm, respectively. Markers represent 48 second bedform averages. Lines projecting from marker represent variability, extending from 8 second average minimum to 8 second maximum values over the 48 second time period.

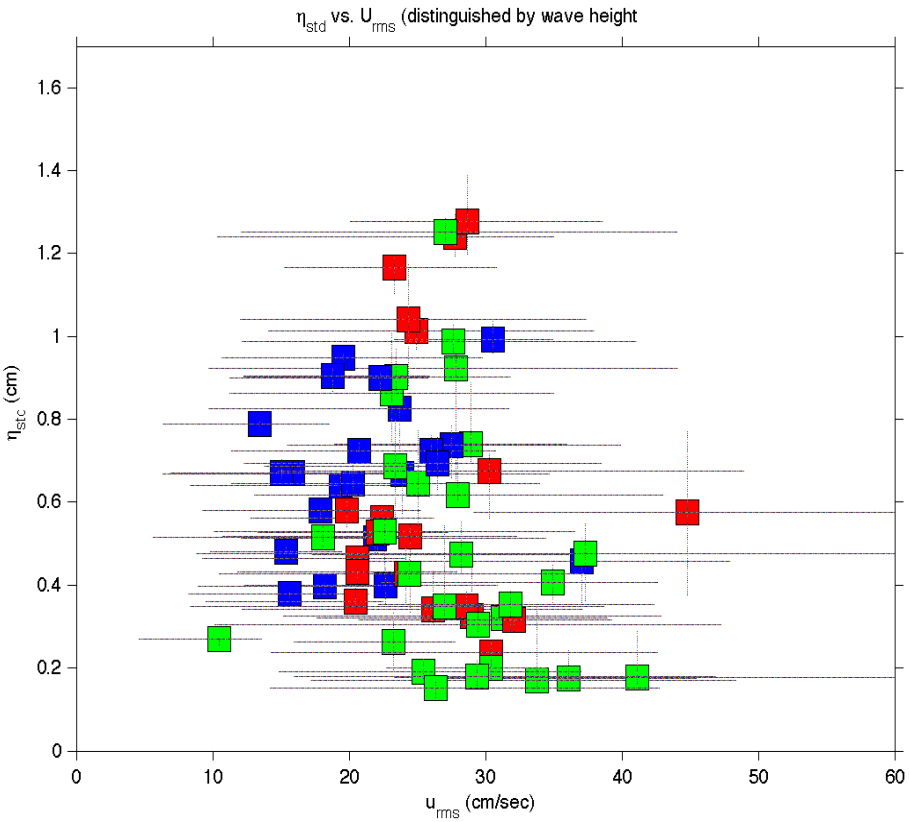

Figure 3.13: η_{std} vs. u_{rms}. Blue, red, and green symbols correspond to observations collected with a significant wave height 30, 40, and 50 cm, respectively. Markers represent 48 second bedform averages. Lines projecting from marker represent variability, extending from 8 second average minimum to 8 second maximum values over the 48 second time period.

CHAPTER 4

CONCLUSIONS

Observations of sea bed geometry were obtained at the O. H. Hinsdale Wave Research Laboratory at Oregon State University as part of a collaborative, large scale laboratory experiment, CROSSTEX. Observations were obtained under random wave conditions using a TMA spectrum with significant wave heights ranging from 30 to 60 cm and wave periods in the range of 4 to 8 seconds. Flow field and seabed geometry data was collected using a submersible PIV system. Both 8 and 48 second average bedform profiles were examined. Sea bed geometry measurements from the 8 and 48 second average bedform profiles include: ripple height, wavelength and radius of curvature, with a primary focus on ripple height and RC. The resulting bed geometries ranged from rippled to flat.

Under a wide variety of wave climates, resulting bedform profiles were found to be quite variable. The sea bed was observed to change significantly over temporal scales as short as one wave group. The 8 second average bedform profiles were found to be much more variable than the longer 48 second averages over the entire PIV sampling time. However, in most instances, 48 second average profiles closely resembled the characteristics of the 8 second average data collected throughout the duration of a 20 minute wave simulation. As the number of observations increased, the 48 second average data was found to more closely correlate to 8 second average profile characteristics. Finally, when all individual geometry

measurements collected throughout an individual wave simulation were averaged, the 8 and 48 second data for RC_{trough} and η_{std} were very similar. This suggests that over long temporal scales, the 48 second bedform characteristics RC_{trough} and η_{std} are representative of the more frequent 8 second average data. The consistency between 8 and 48 second bedform average characteristics does not exist for RC_{crest}. Forty-eight second RC_{crest} observations tend to be larger than the 48 second measurements. The relatively short response time of RC_{crest} and large amount of variability has shown that the crest often goes from peaky to a gentle crest over short temporal scales. The peakiness of RC_{crest} over short intervals is represented in 8 second average data, revealed by smaller values of RC. However, as the RC_{crest} responds rapidly to hydrodynamic forcing, 48 seconds proves to be too great of an averaging window, and peaky to gentle crested RC_{crest} modulations are not able to be observed. This results in larger 48 second values of RC_{crest}, consistent with a flatter, less peaky bed.

No significant claims can be made about λ_b. Bedform wavelength data was found to be independent of u_{rms}, significant wave height, and peak wave period.

RC_{crest} and RC_{trough} are found to increase with increasing u_{rms}. There is no significant correlation between wave period and RC, suggesting that peak period has no effect on ripple height. RC is dependent on significant wave height. For similar values of u_{rms}, resulting RC is larger under conditions of larger wave heights.

Conversely, η_{std} is dependent on wave peak period. Ripple height shows a strong inverse relationship to u_{rms} when the bed responds to relatively large peak periods of 6 and 8 seconds. For small wave peak period values of 4 seconds, η_{std} is independent of u_{rms}. η_{std} values for the small wave peak periods tend to be much larger for similar root-mean-square velocities observed with larger wave periods.

Additional investigation into the effect of wave height and peak period on ripple geometry characteristics could provide further insight into sedimentary structures in the nearshore.

APPENDIX A

ADDITIONAL FIGURES

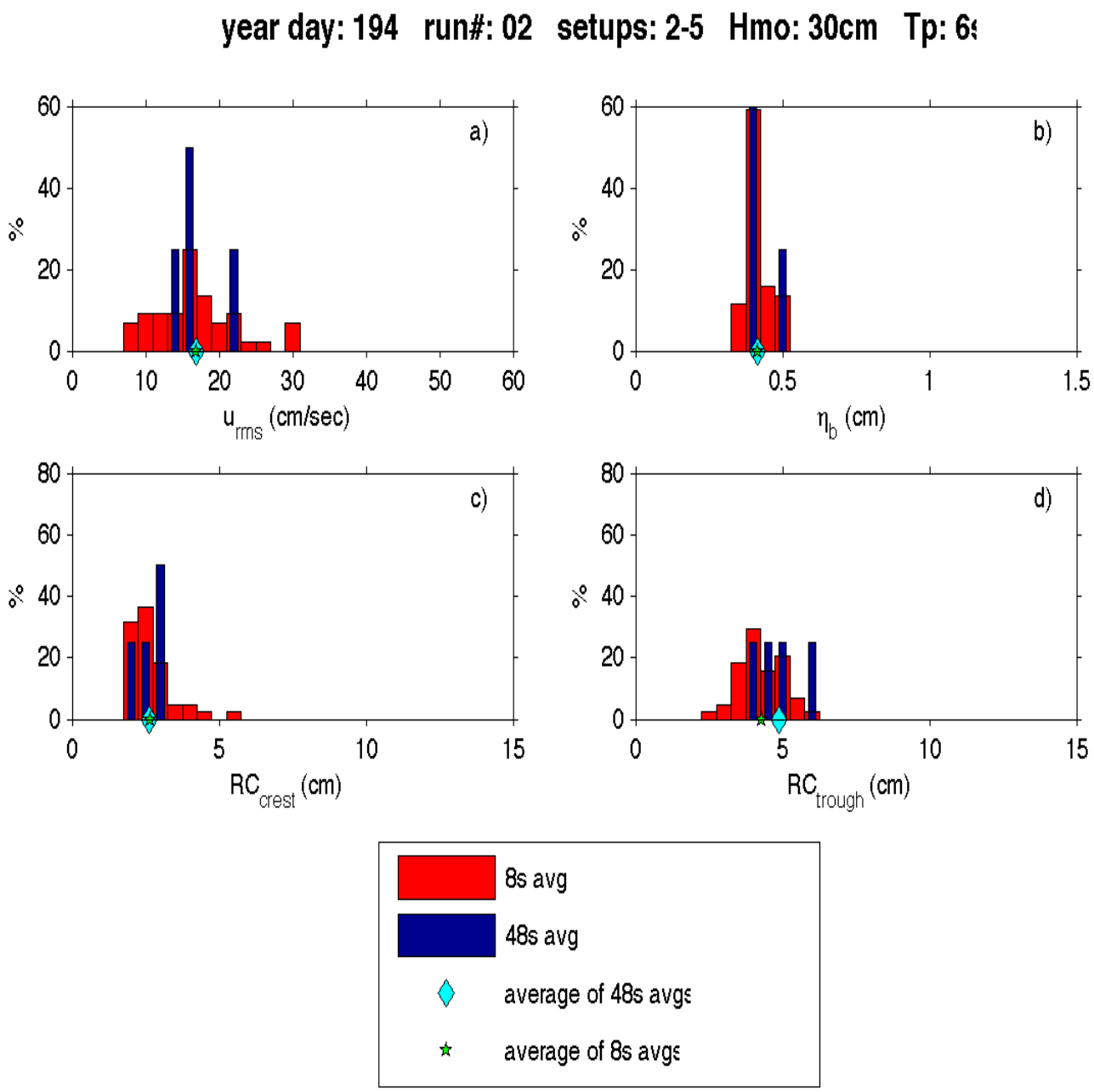

Figure A.1: Histogram. y-axis percentage, fixed

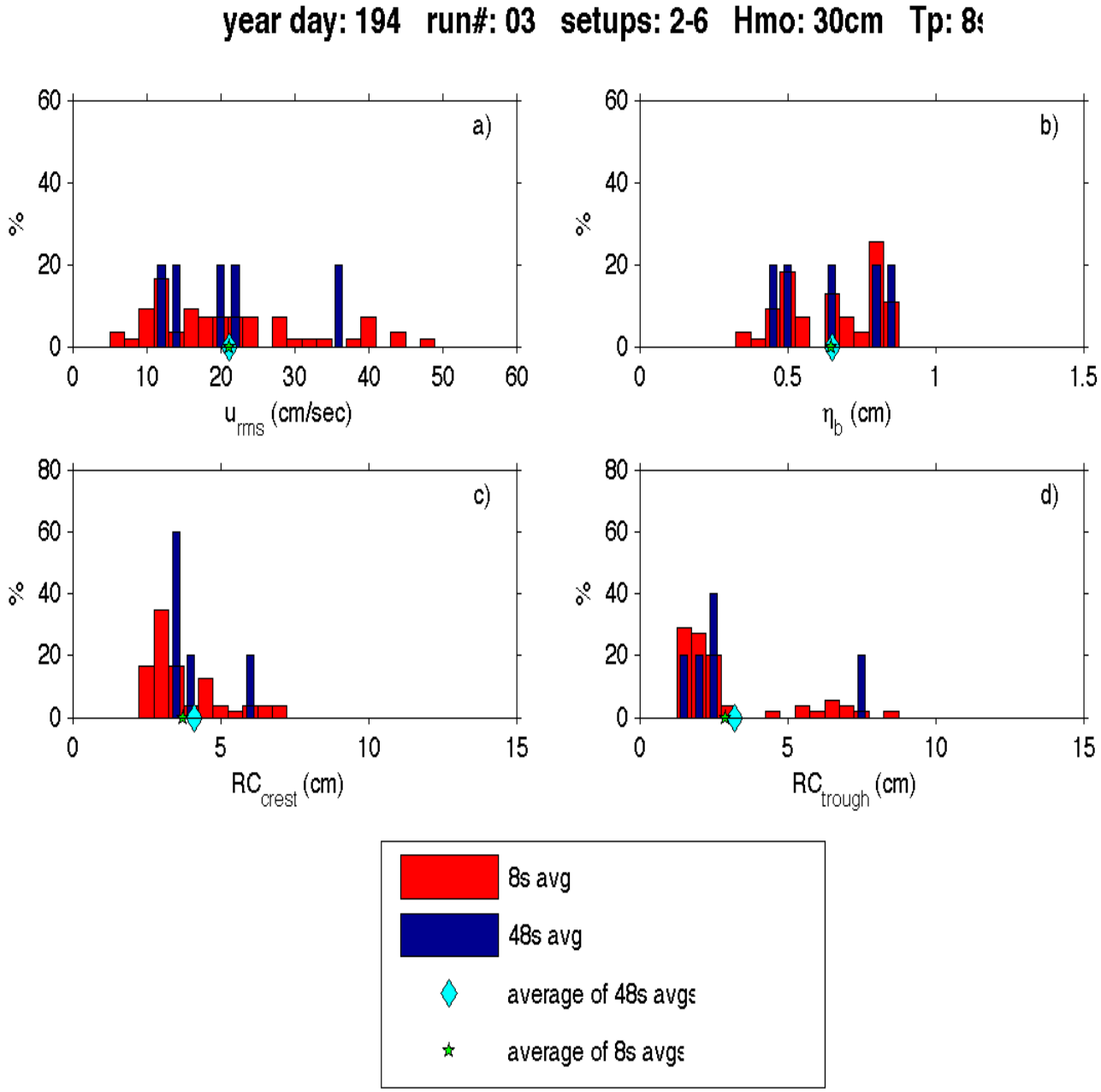

Figure A.2: Histogram. y-axis percentage, fixed

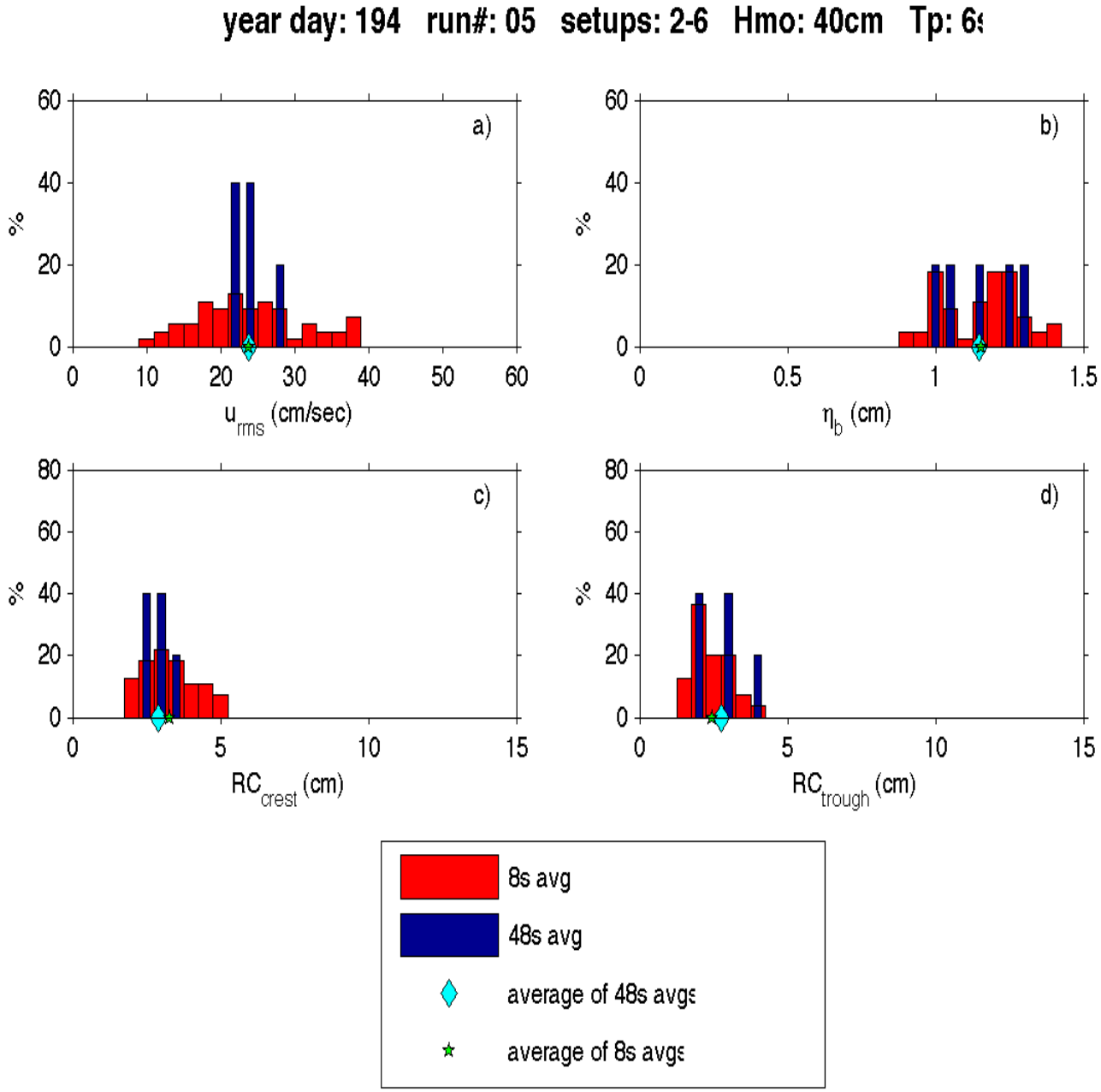

Figure A.3: Histogram. y-axis percentage, fixed

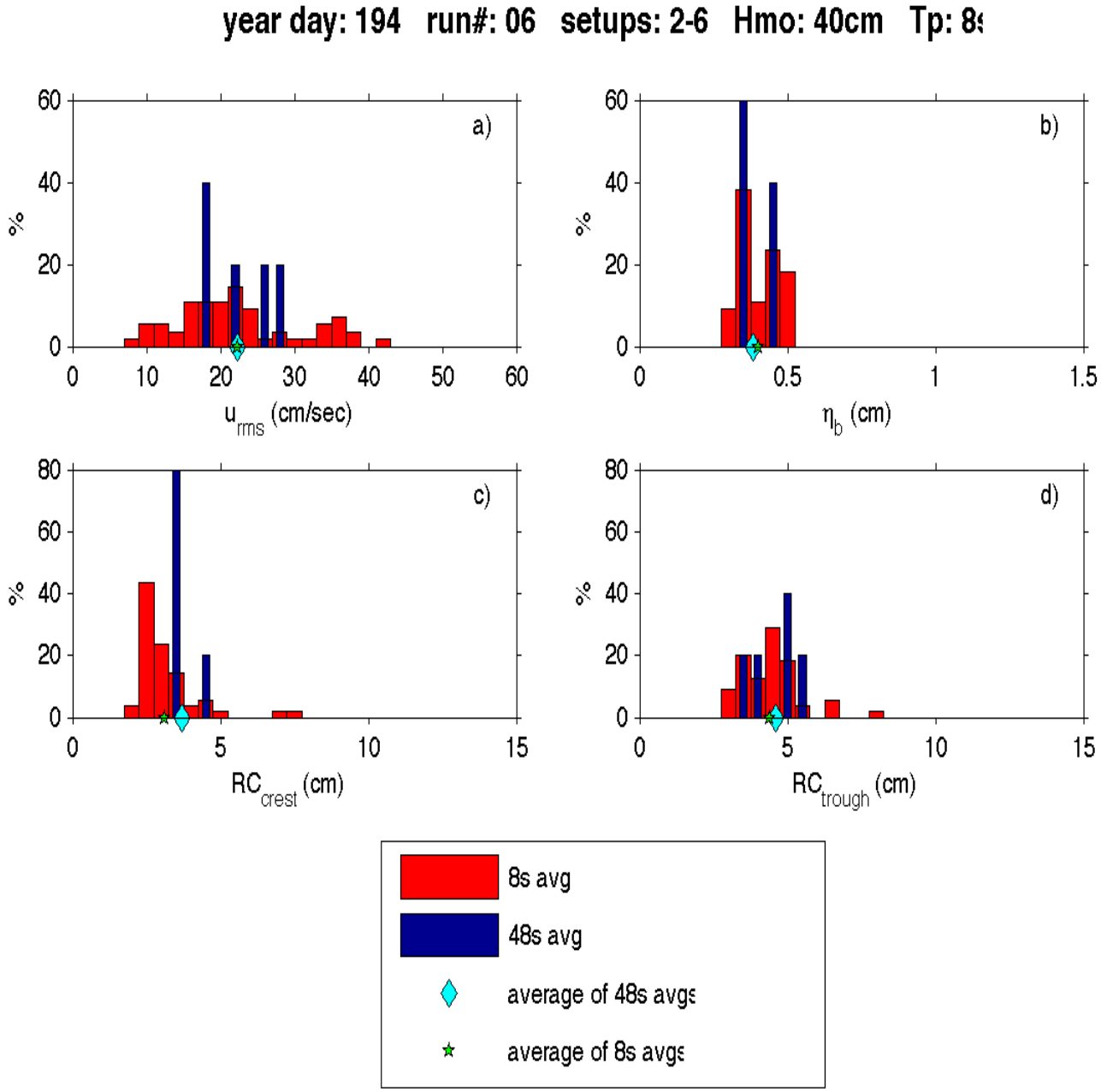

Figure A.4: Histogram. y-axis percentage, fixed

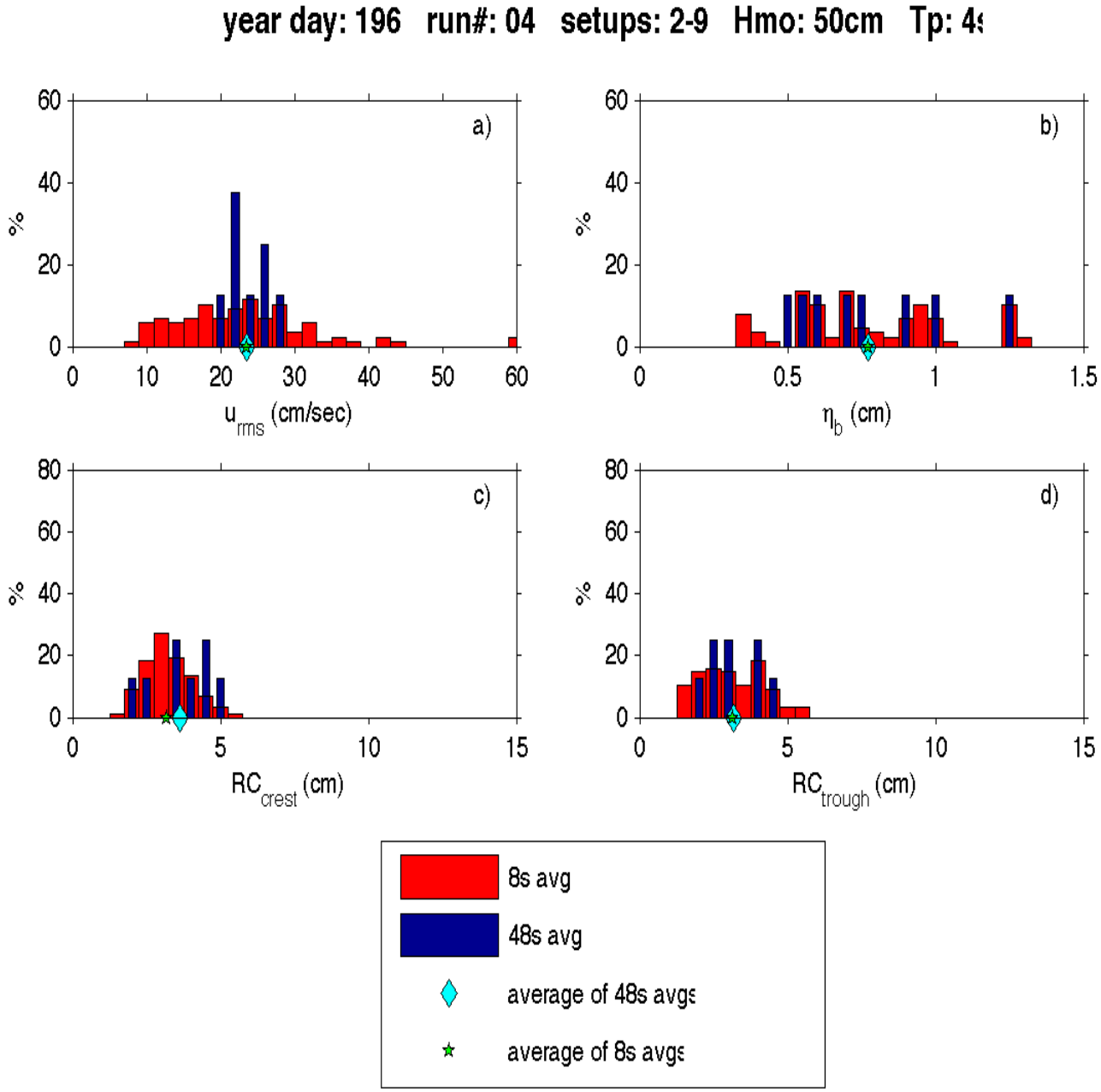

Figure A.5: Histogram. y-axis percentage, fixed

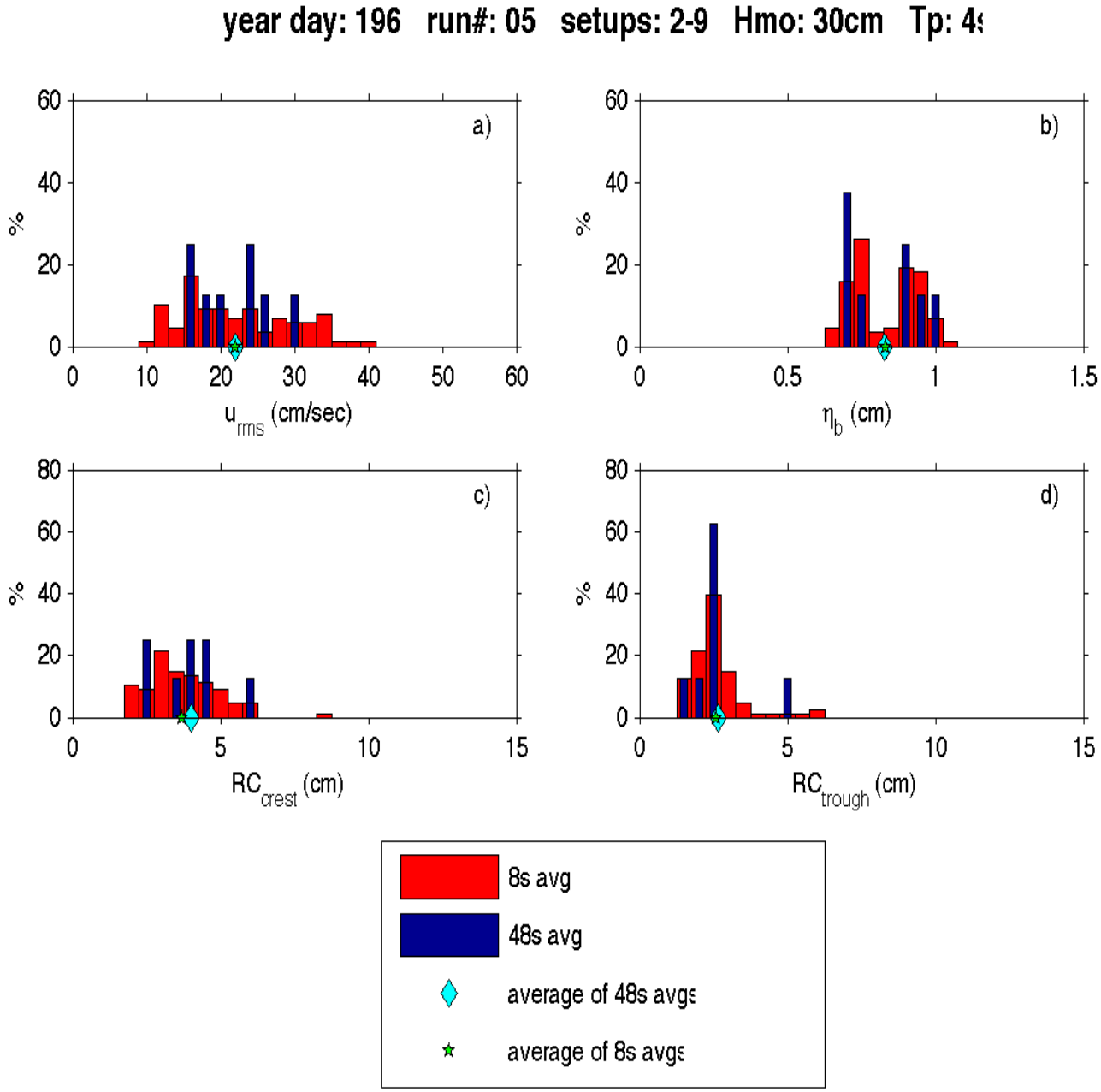

Figure A.6: Histogram. y-axis percentage, fixed

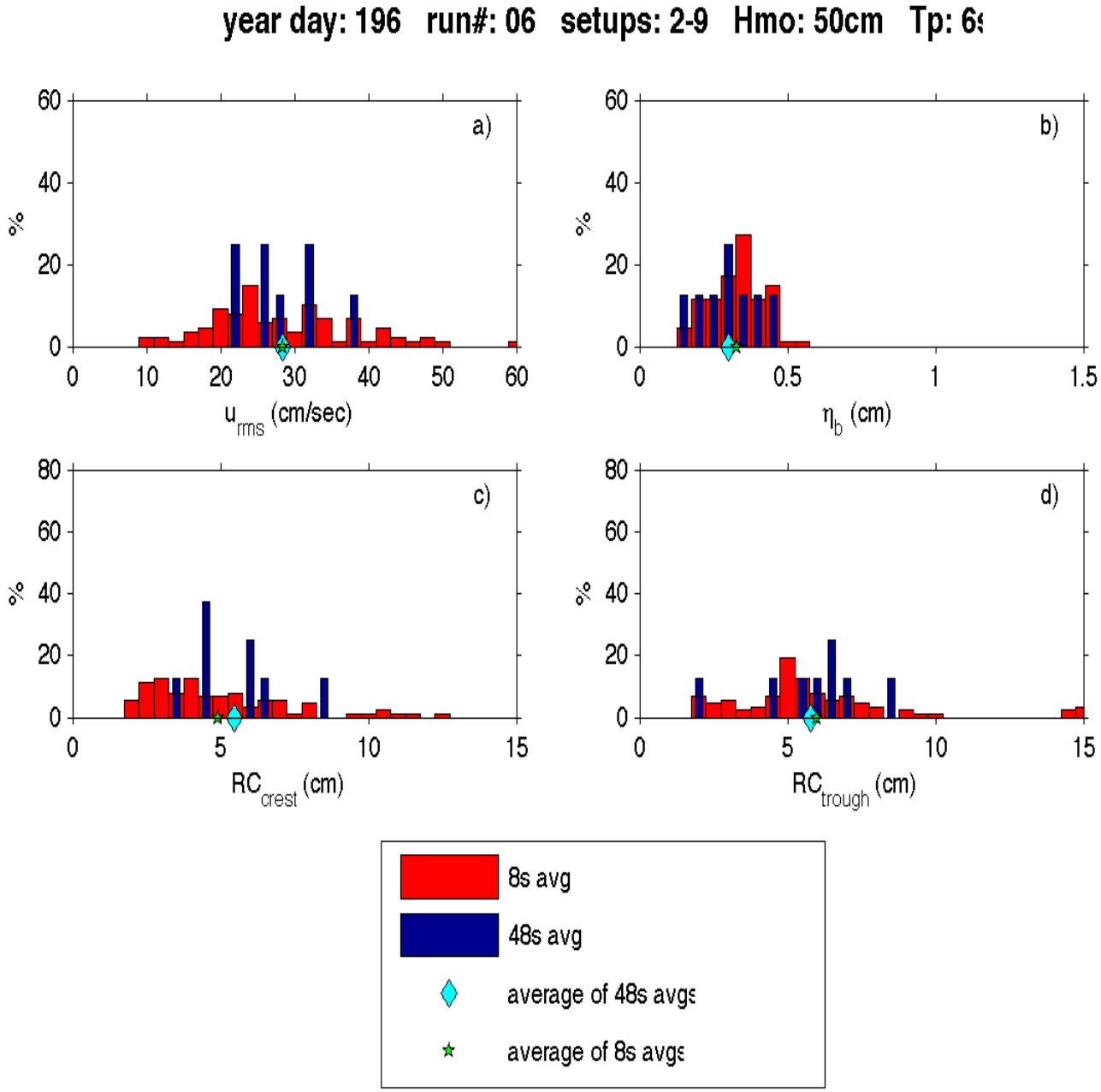

Figure A.7: Histogram. y-axis percentage, fixed

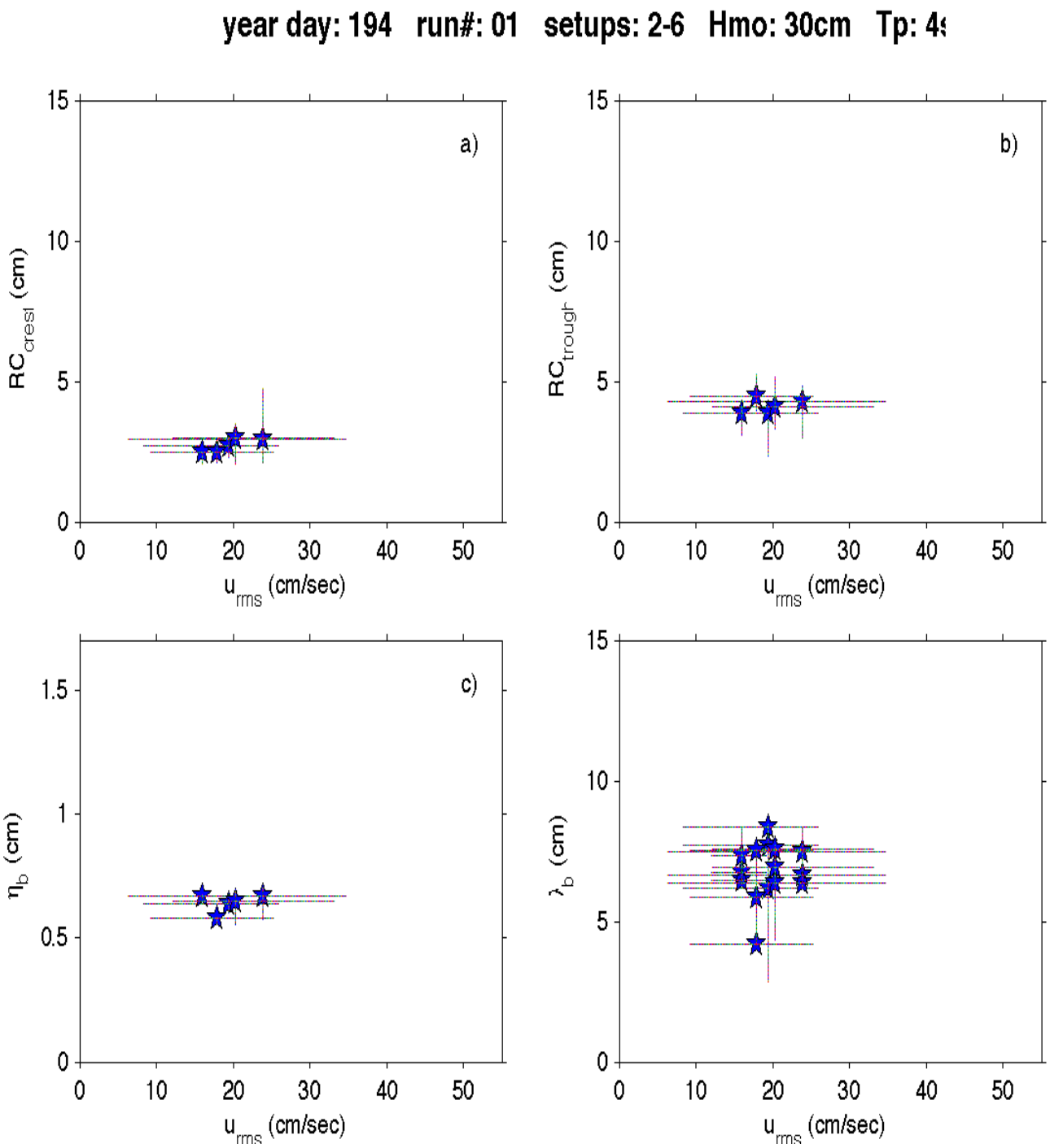

Figure A.8: Bed state characteristics versus root-mean-square velocity.

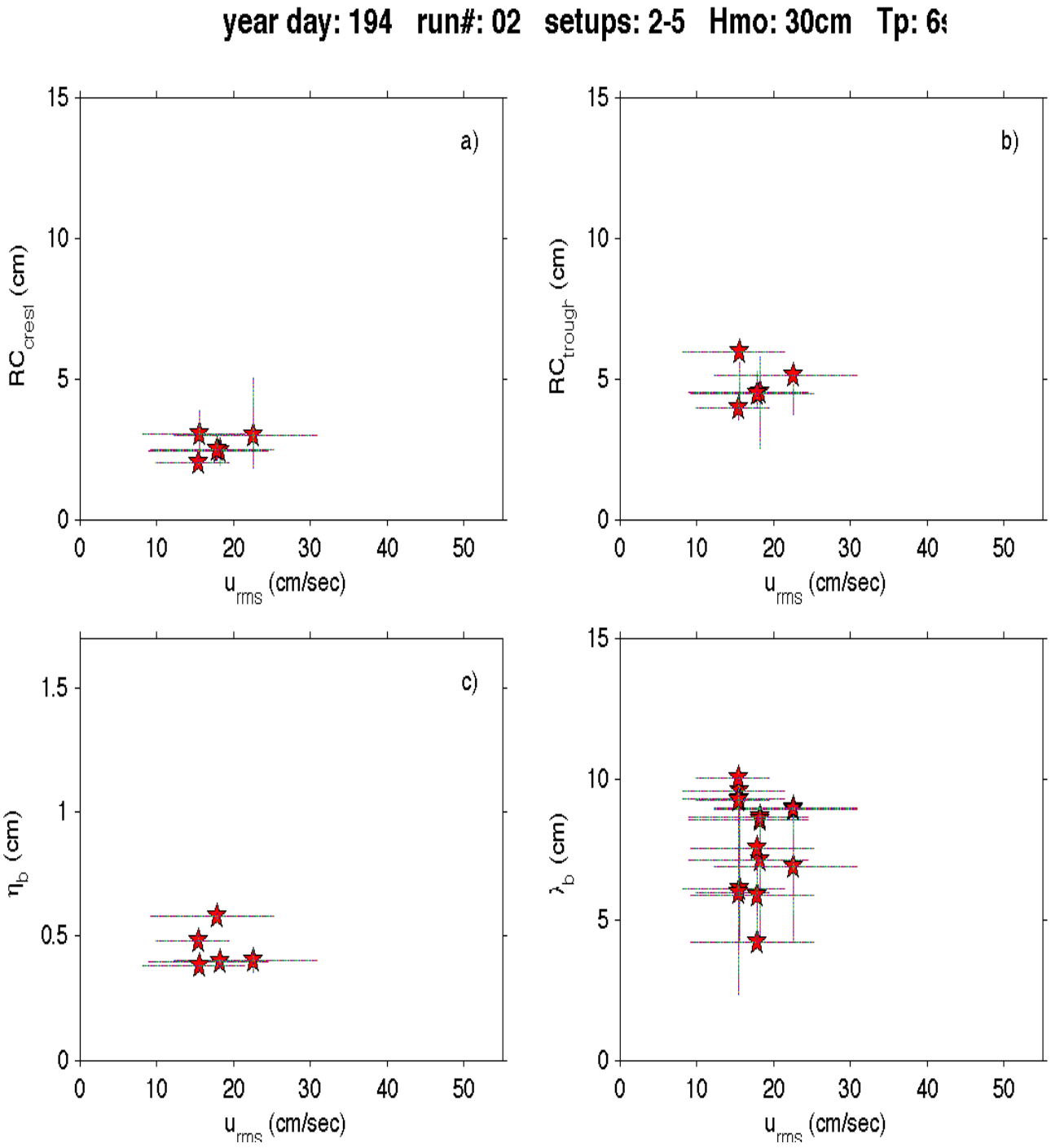

Figure A.9: Bed state characteristics versus root-mean-square velocity.

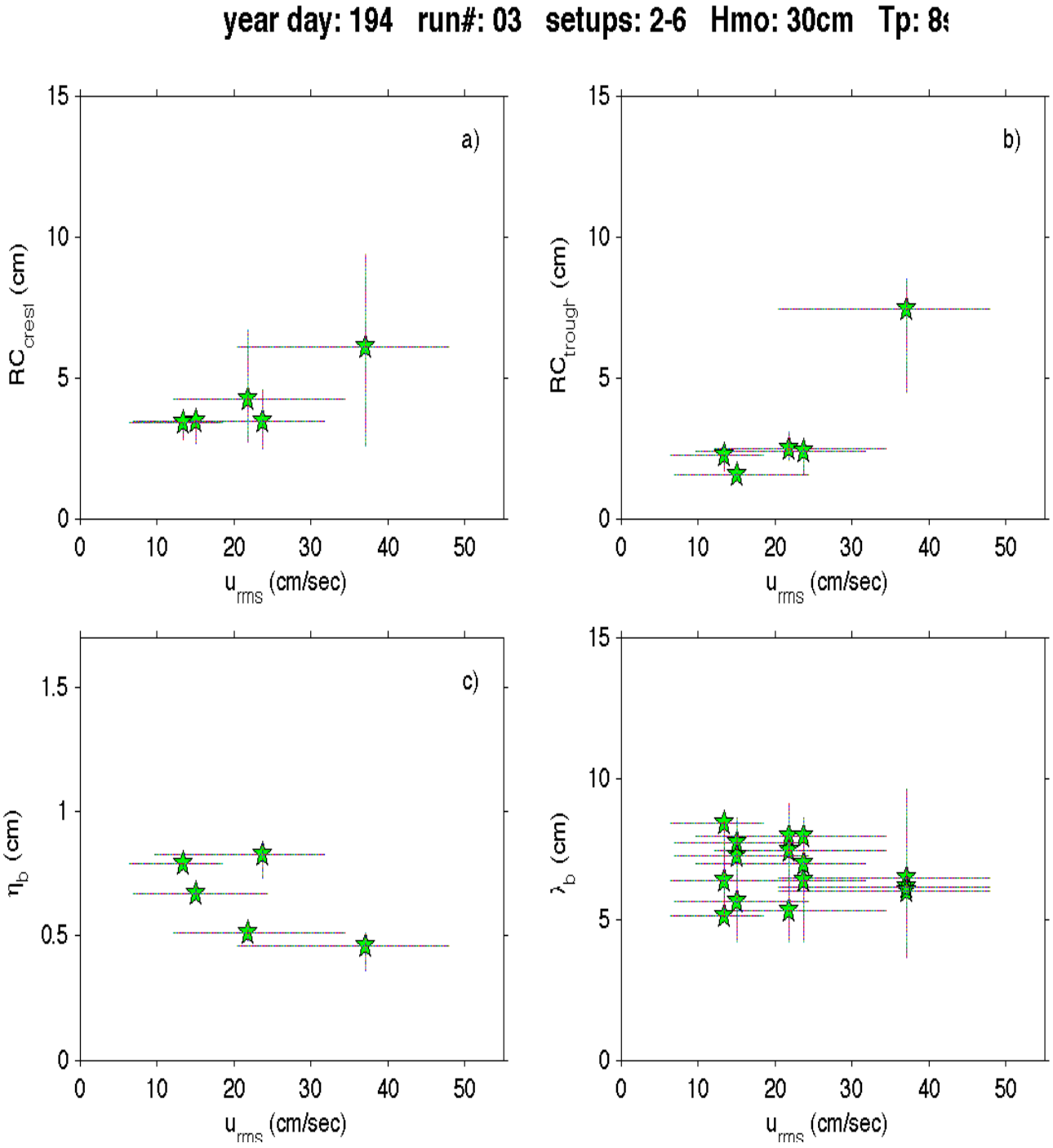

Figure A.10: Bed state characteristics versus root-mean-square velocity.

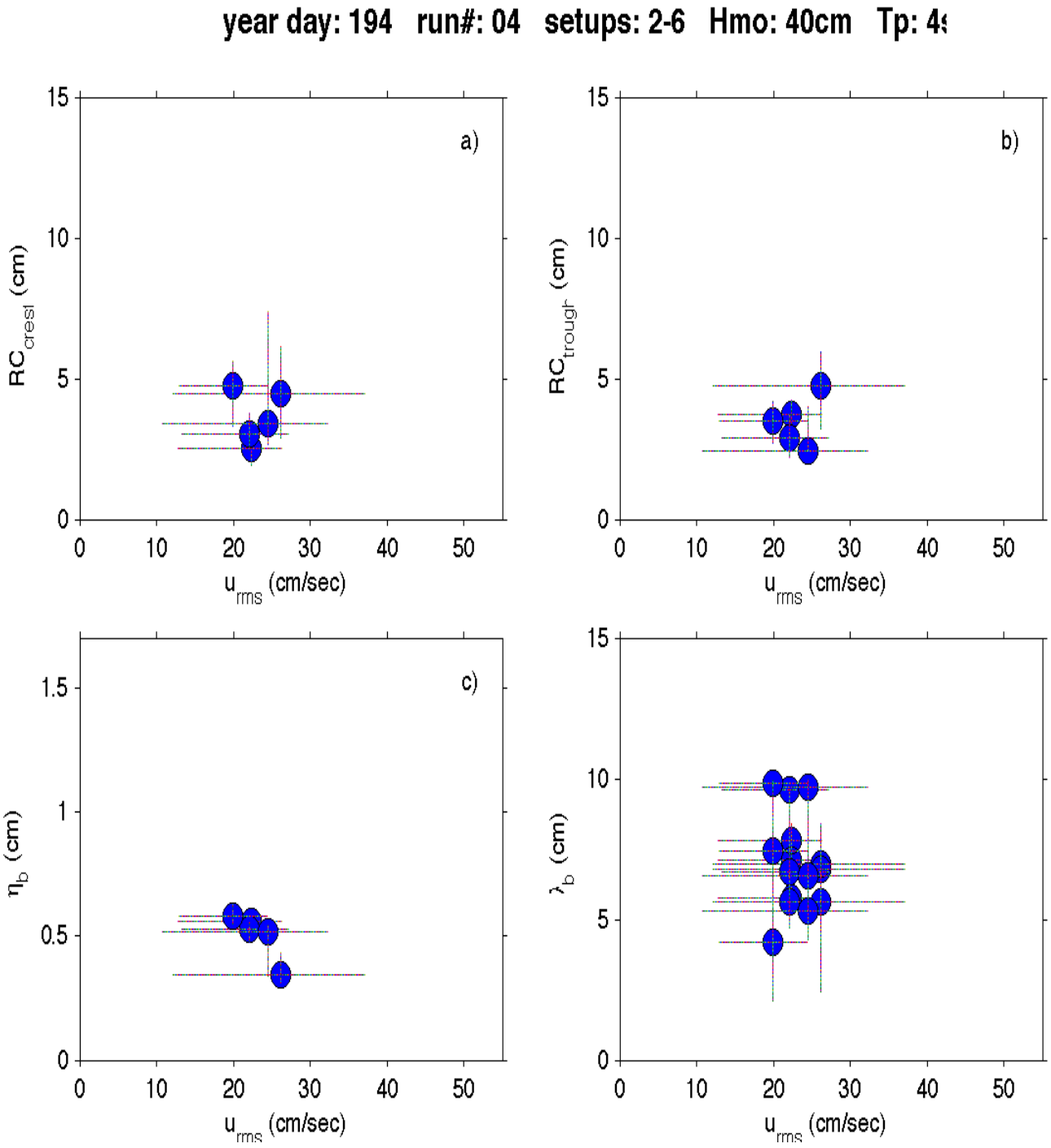

Figure A.11: Bed state characteristics versus root-mean-square velocity.

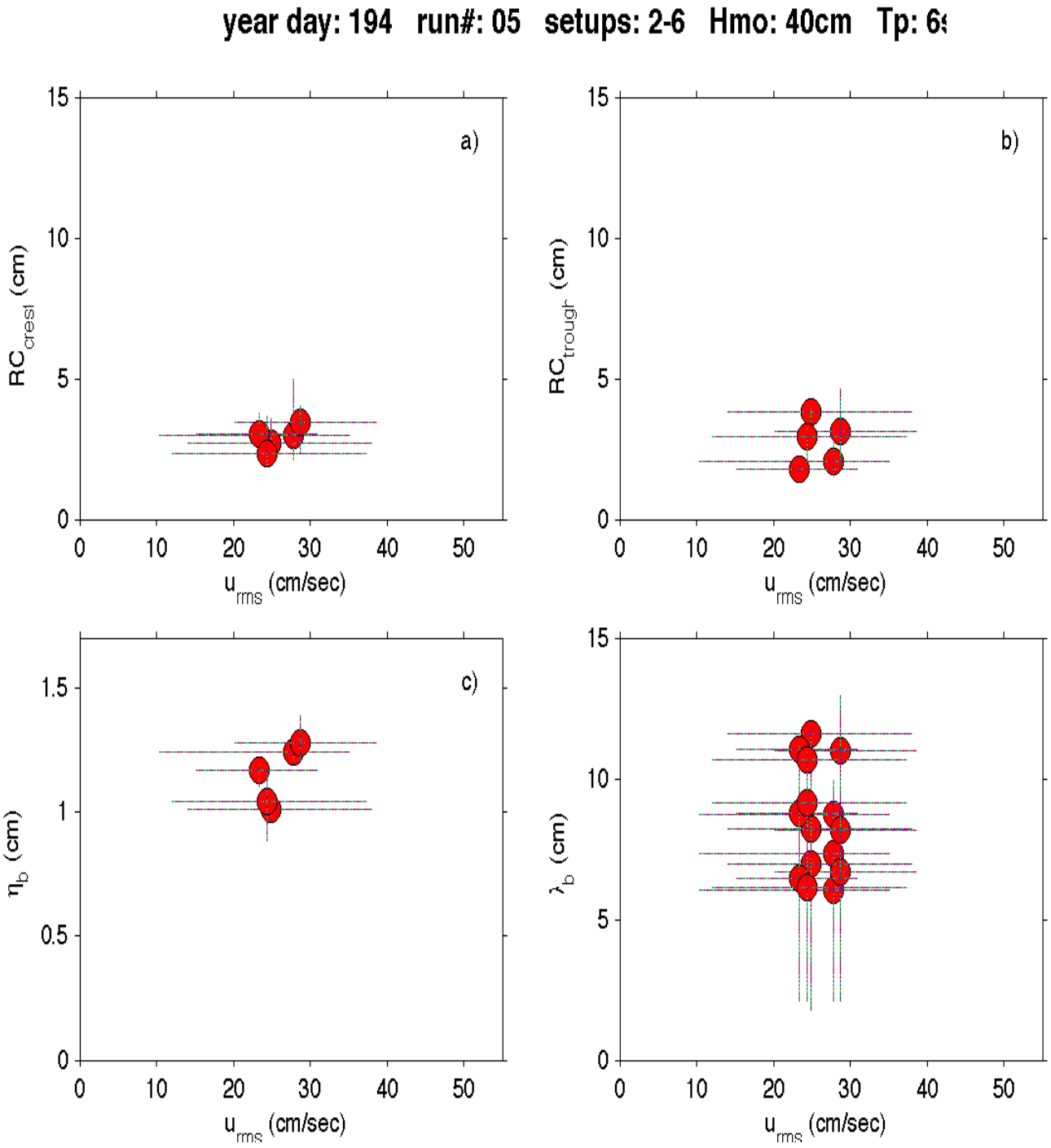

Figure A.12: Bed state characteristics versus root-mean-square velocity.

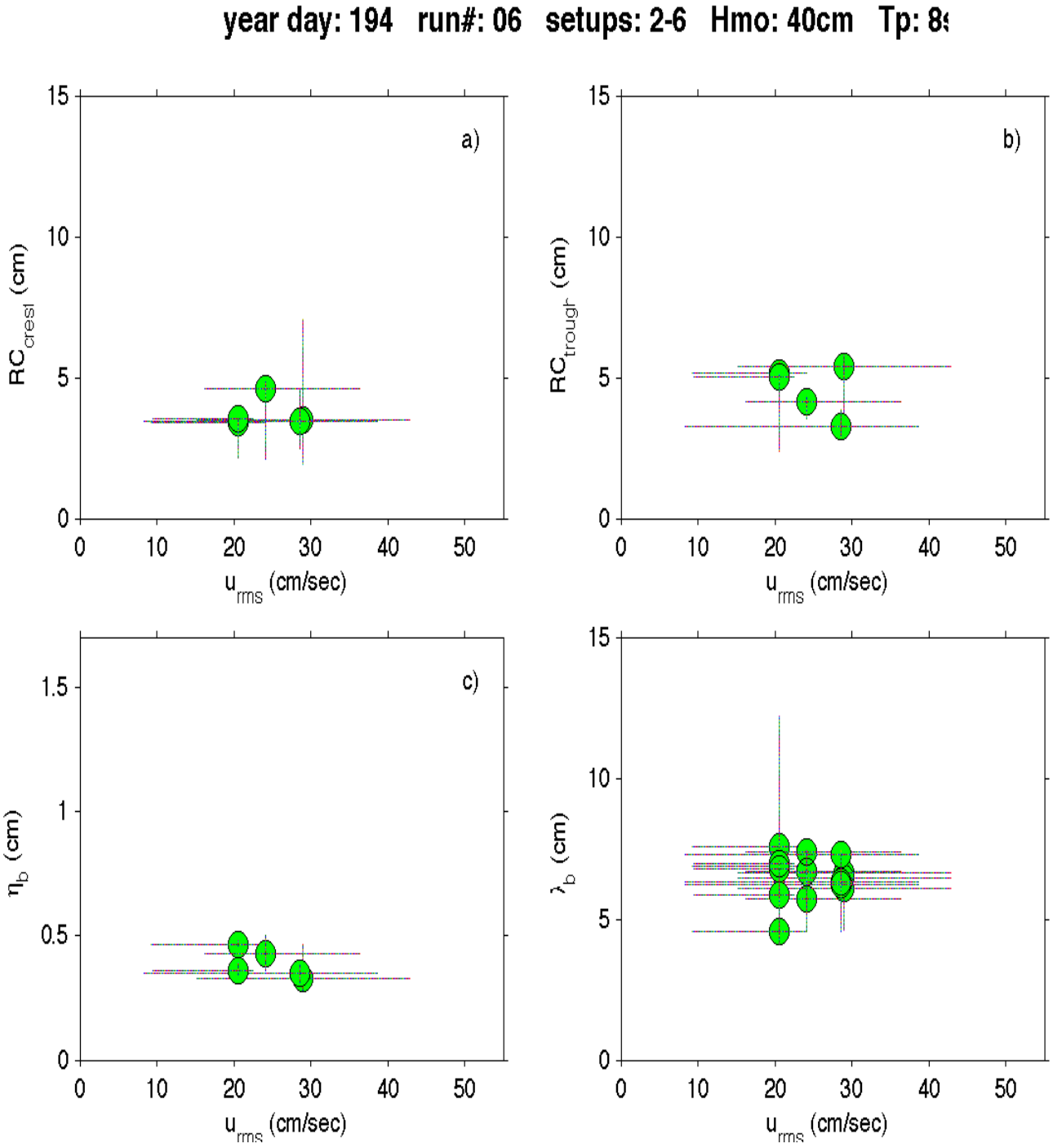

Figure A.13: Bed state characteristics versus root-mean-square velocity.

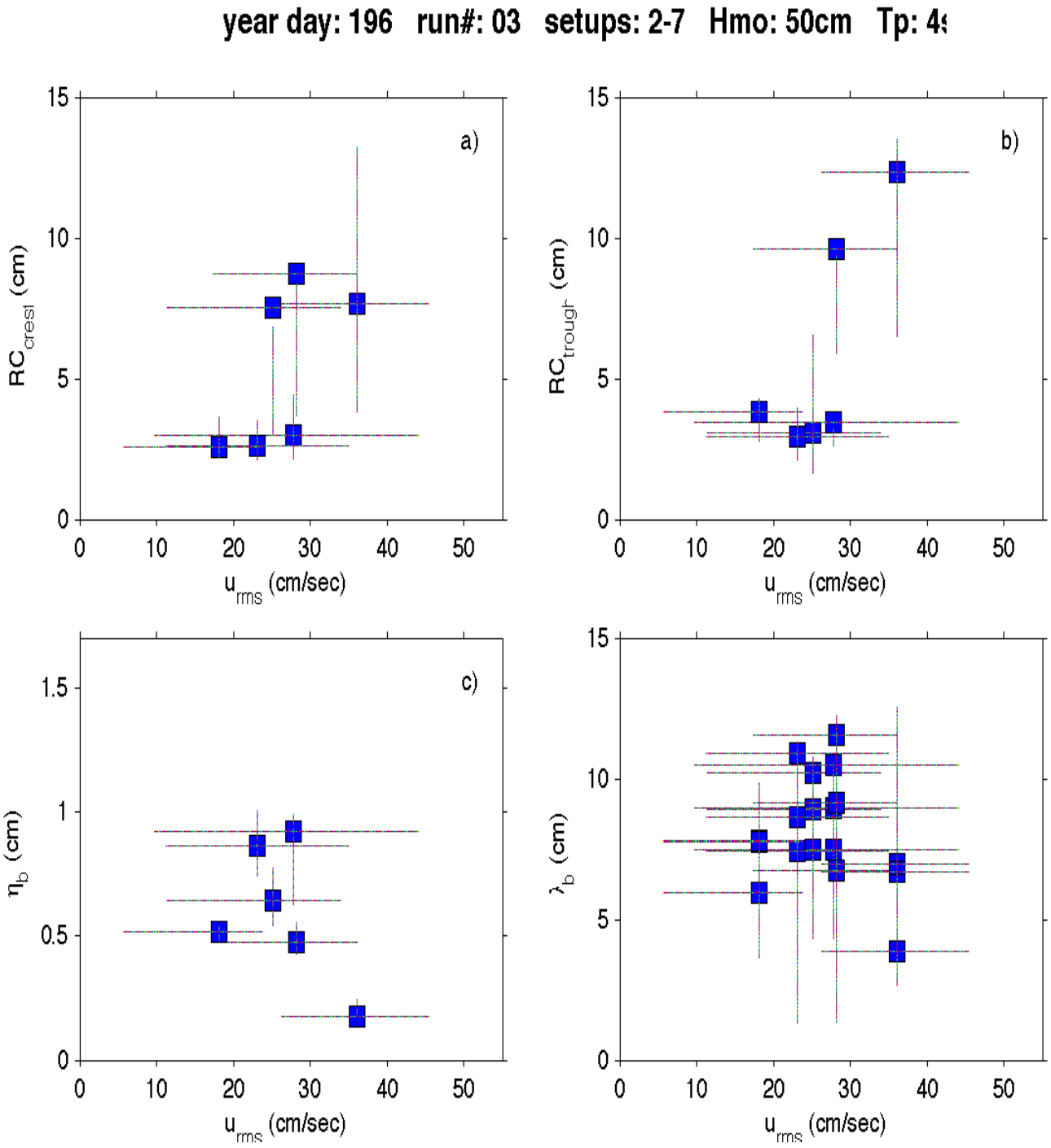

Figure A.14: Bed state characteristics versus root-mean-square velocity.

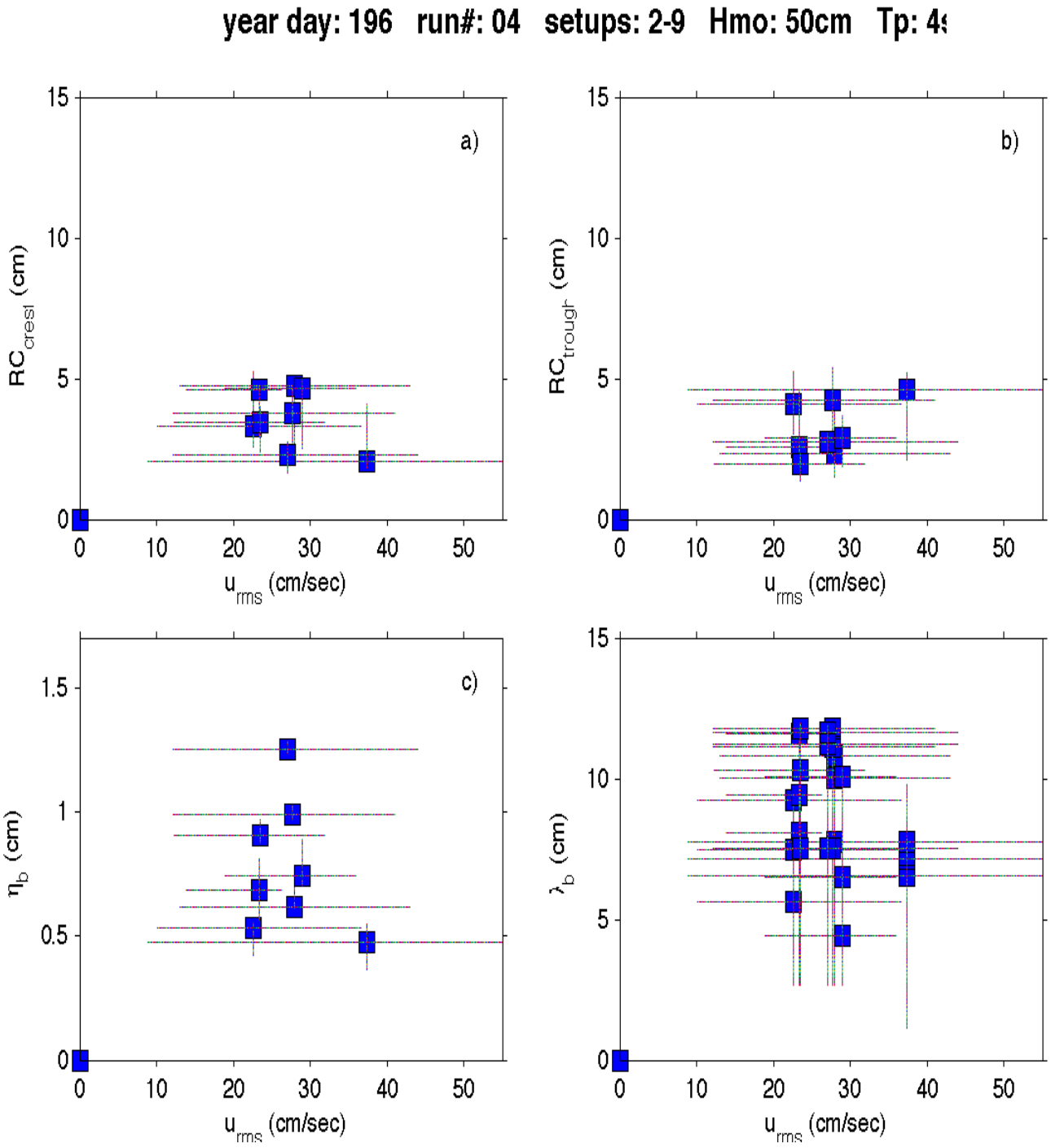

Figure A.15: Bed state characteristics versus root-mean-square velocity.

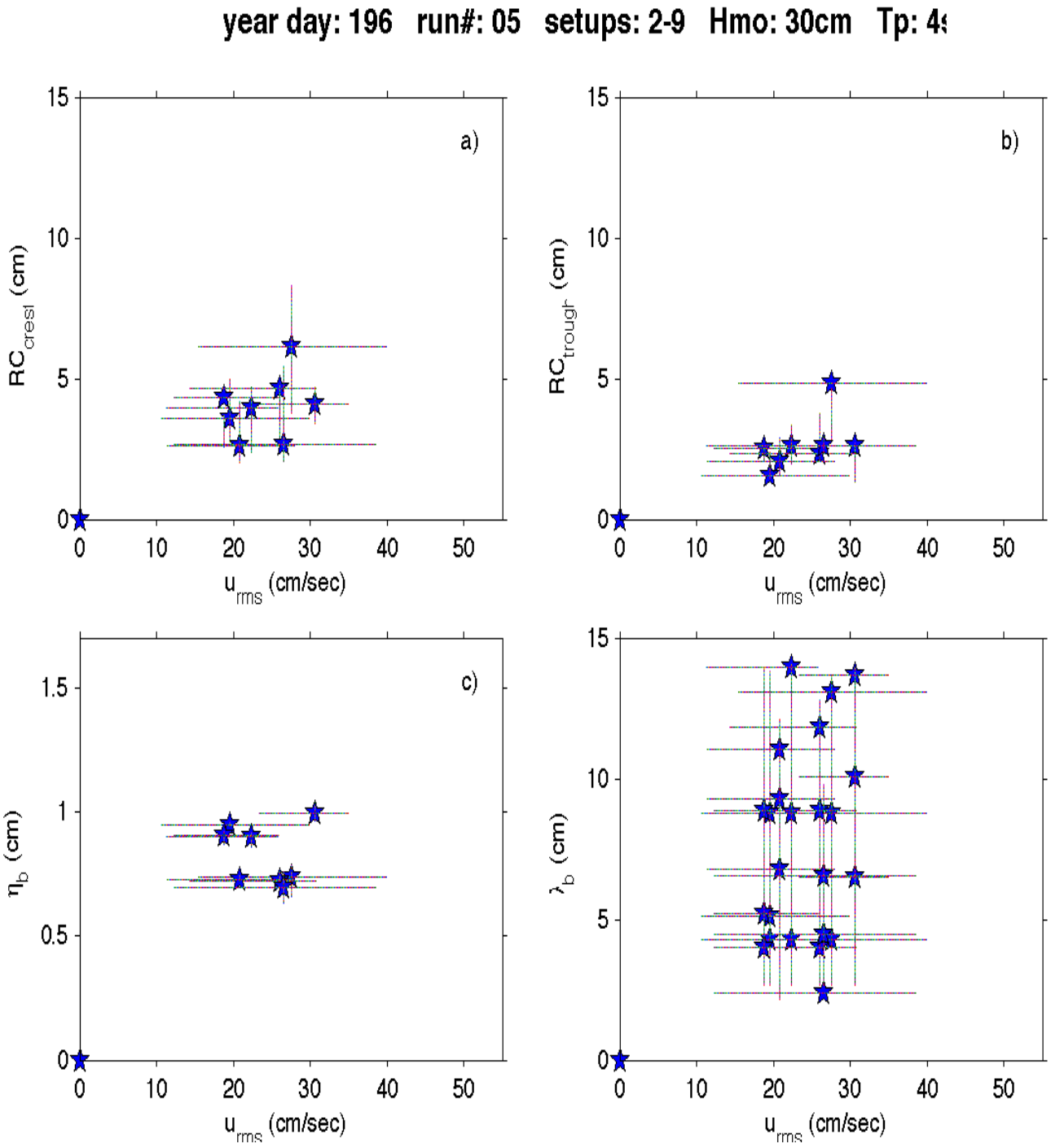

Figure A.16: Bed state characteristics versus root-mean-square velocity.

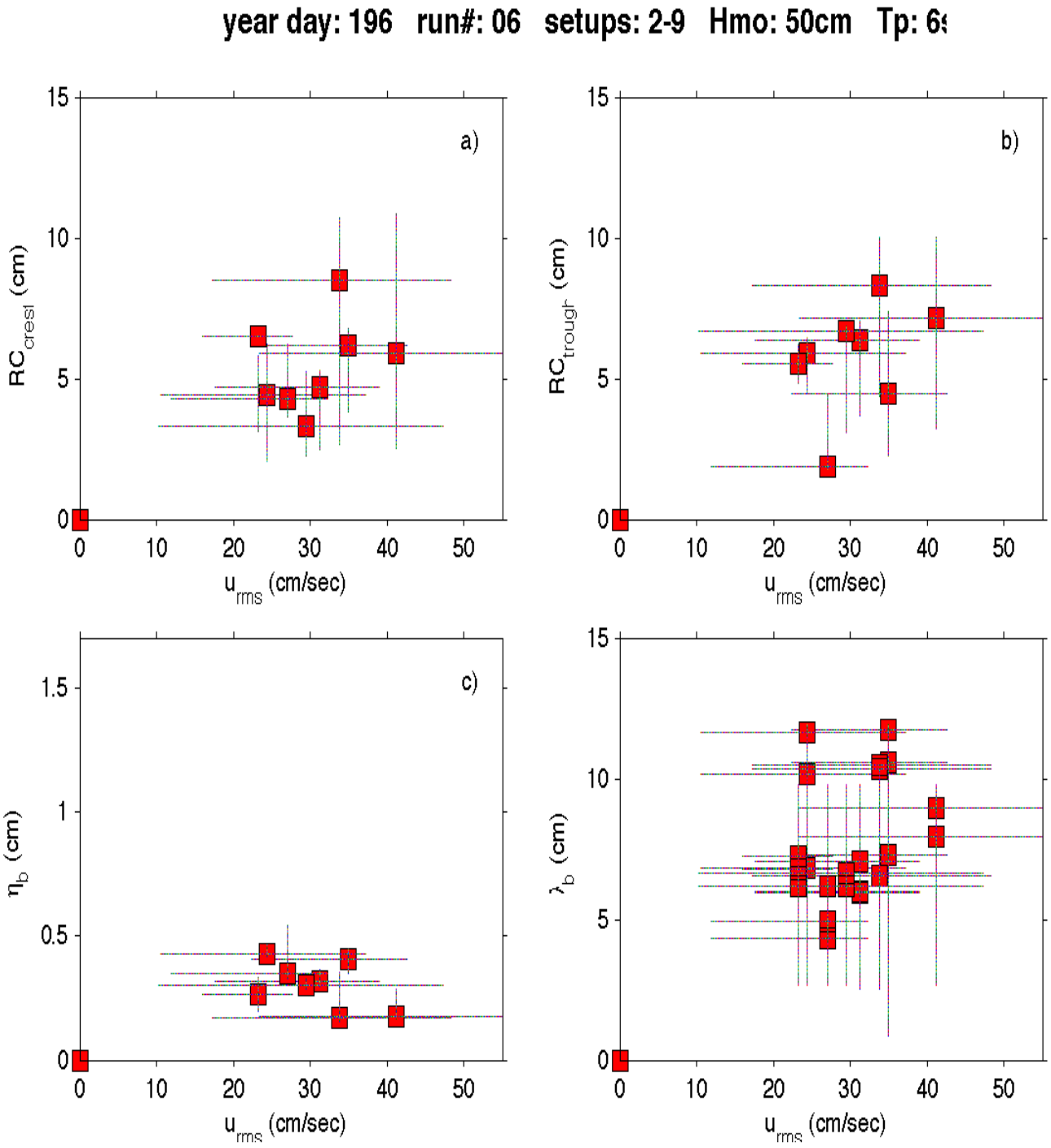

Figure A.17: Bed state characteristics versus root-mean-square velocity.

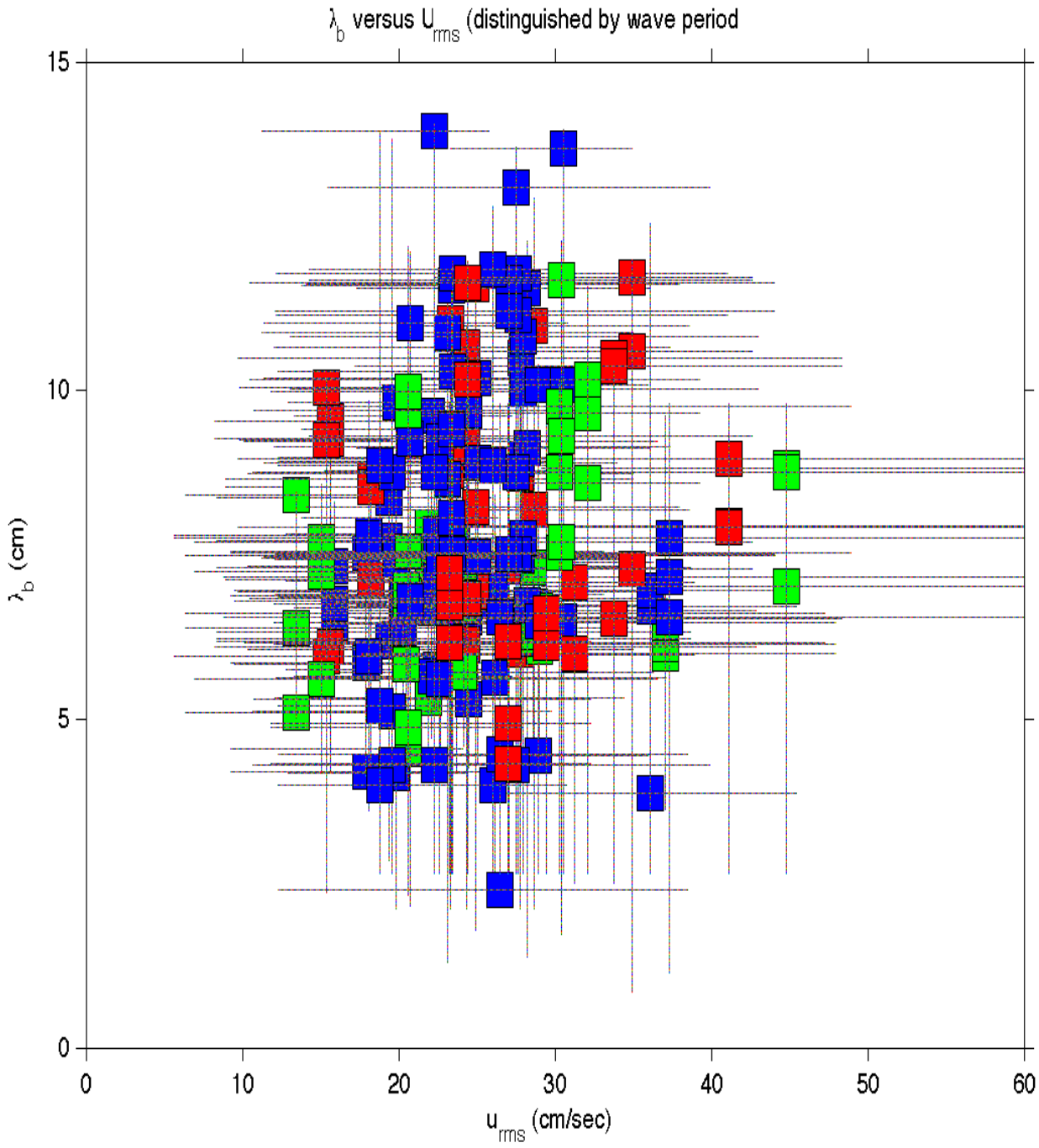

Figure A.18: λ_b vs. u_{rms}. Blue symbols correspond to observations collected with a wave period of 4s. Red symbols correspond to a 6s period and green markers correspond to a period of 8s. Marker represents 48 second bedform averages. Lines extend from 8 second average minimum to 8 second maximum values.

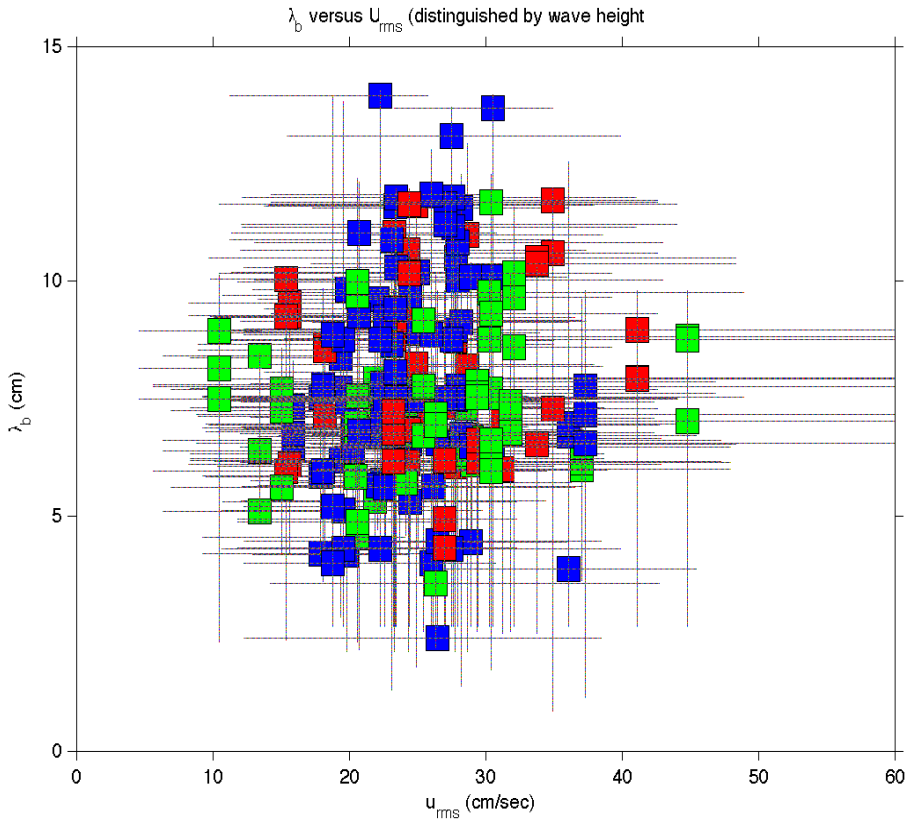

Figure A.19: RC_t vs. u_{rms}. Blue, red, and green symbols correspond to observations collected with a wave Height 30 cm, 40 cm, and 50 cm, respectively. Markers represent 48 second bedform averages. Lines projecting from marker represent variability, extending from 8 second average minimum to 8 second maximum values over the 48 second time period.

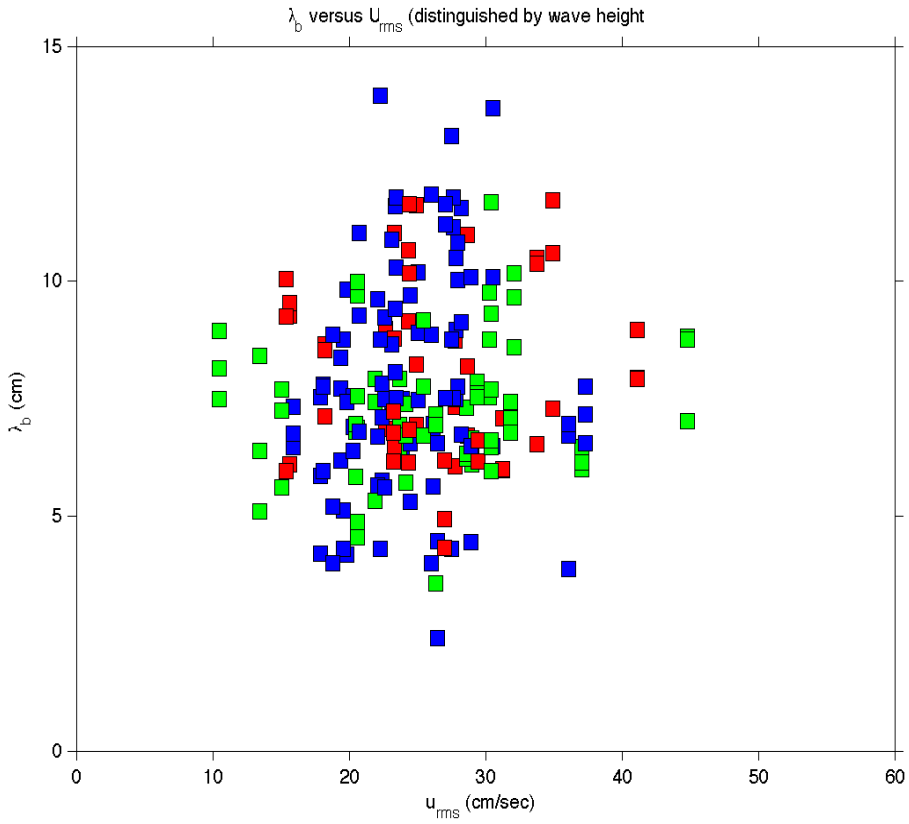

Figure A.20: RC_t vs. U_{rms}. Blue, red, and green symbols correspond to observations collected with a wave Height 30 cm, 40 cm, and 50 cm, respectively. Markers represent 48 second bedform averages.

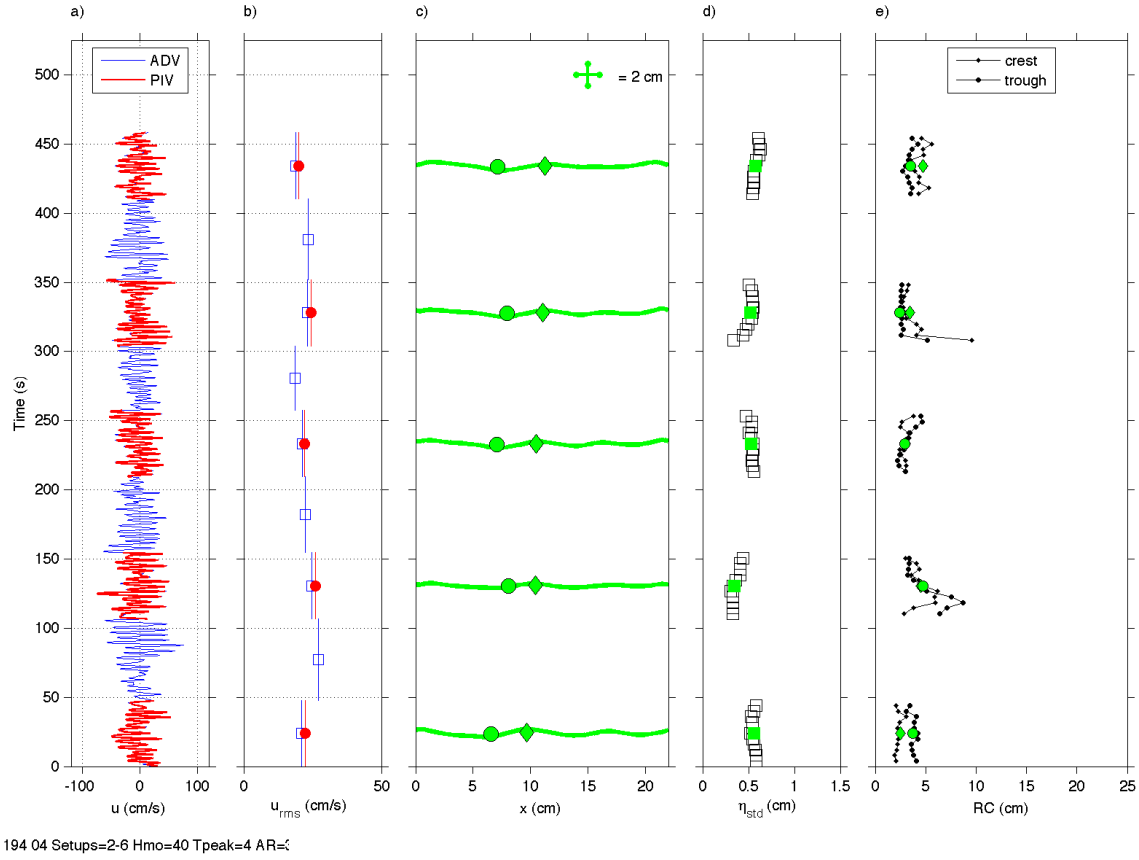

Figure A.21: Velocity and sea bed geometry resulting from 40 cm significant wave height and 8 second peak period. a) Velocity data as collected by the PIV system (red) and ADV (blue). b) Root-mean-square velocity over 48 second time intervals, using the same color scheme as a). 48 second average bed forms are depicted in c). Diamond and circular markers on each bed form reveal the location of the crest and trough locations used for RC measurements. d) Ripple height for 8 (black) and 48 (green) second average bedforms. e) RC measurements for 8 (black) and 48 (green) second average bedforms.

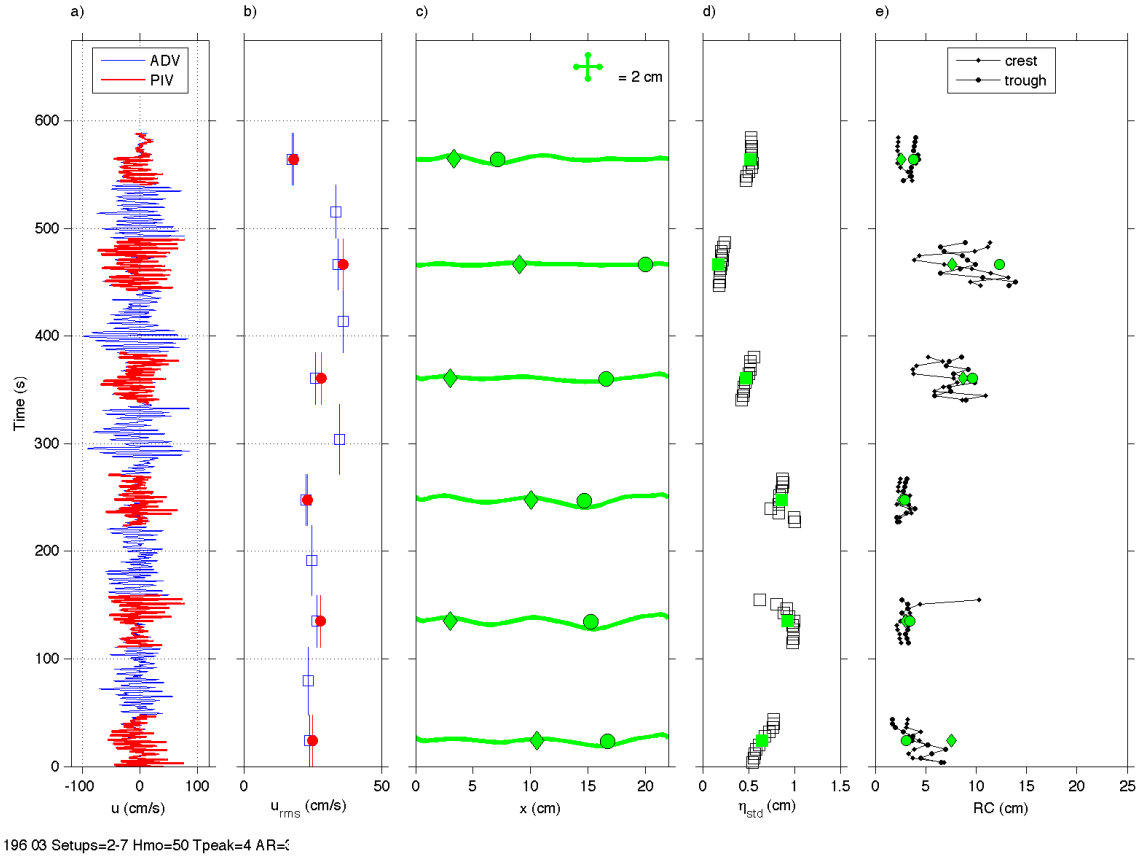

Figure A.22: Velocity and sea bed geometry resulting from 40 cm significant wave height and 8 second peak period. a) Velocity data as collected by the PIV system (red) and ADV (blue). b) Root-mean-square velocity over 48 second time intervals, using the same color scheme as a). 48 second average bed forms are depicted in c). Diamond and circular markers on each bed form reveal the location of the crest and trough locations used for RC measurements. d) Ripple height for 8 (black) and 48 (green) second average bedforms. e) RC measurements for 8 (black) and 48 (green) second average bedforms.

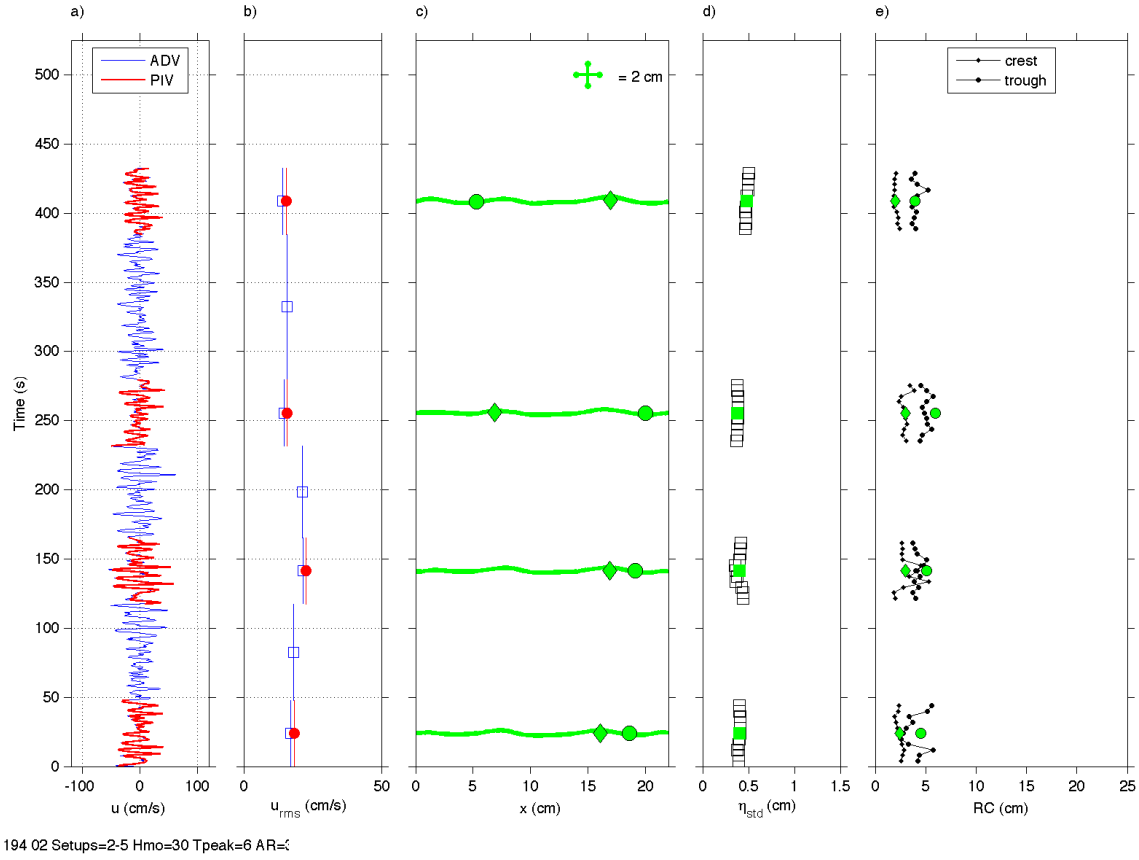

Figure A.23: Velocity and sea bed geometry resulting from 40 cm significant wave height and 8 second peak period. a) Velocity data as collected by the PIV system (red) and ADV (blue). b) Root-mean-square velocity over 48 second time intervals, using the same color scheme as a). 48 second average bed forms are depicted in c). Diamond and circular markers on each bed form reveal the location of the crest and trough locations used for RC measurements. d) Ripple height for 8 (black) and 48 (green) second average bedforms. e) RC measurements for 8 (black) and 48 (green) second average bedforms.

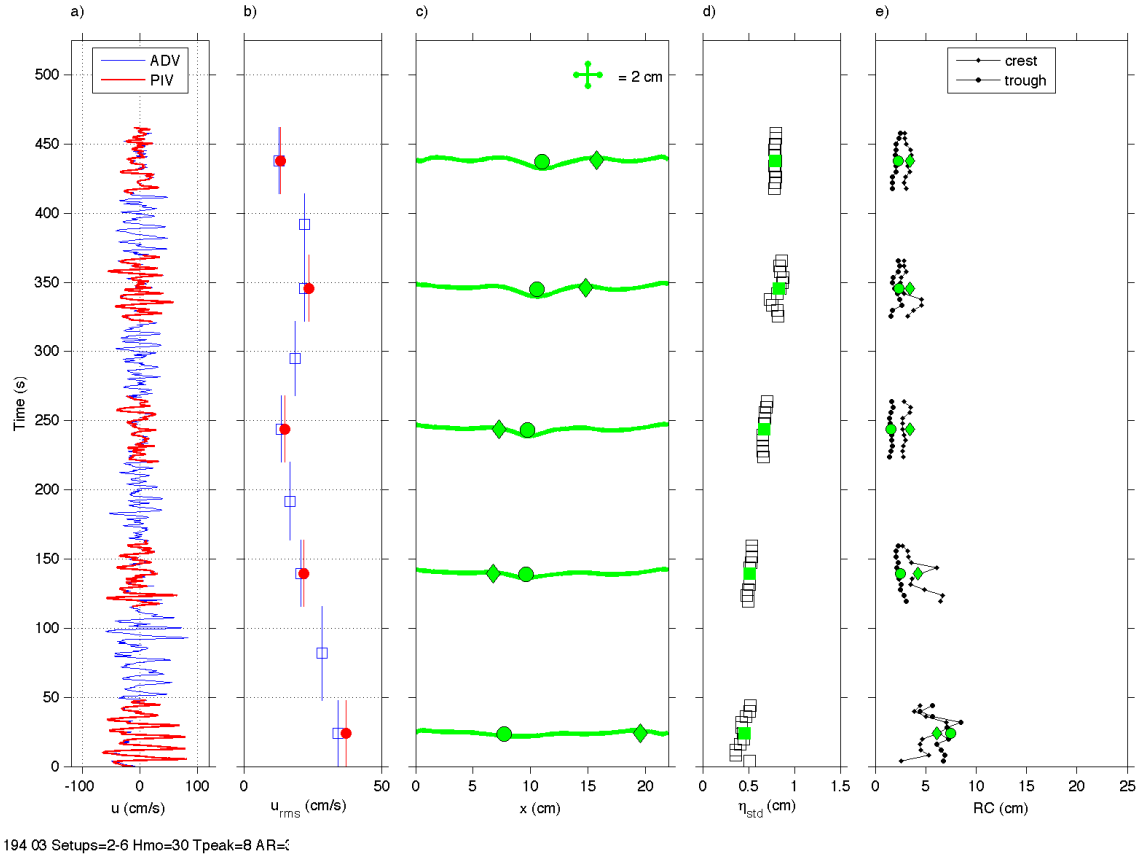

Figure A.24: Velocity and sea bed geometry resulting from 40 cm significant wave height and 8 second peak period. a) Velocity data as collected by the PIV system (red) and ADV (blue). b) Root-mean-square velocity over 48 second time intervals, using the same color scheme as a). 48 second average bed forms are depicted in c). Diamond and circular markers on each bed form reveal the location of the crest and trough locations used for RC measurements. d) Ripple height for 8 (black) and 48 (green) second average bedforms. e) RC measurements for 8 (black) and 48 (green) second average bedforms.

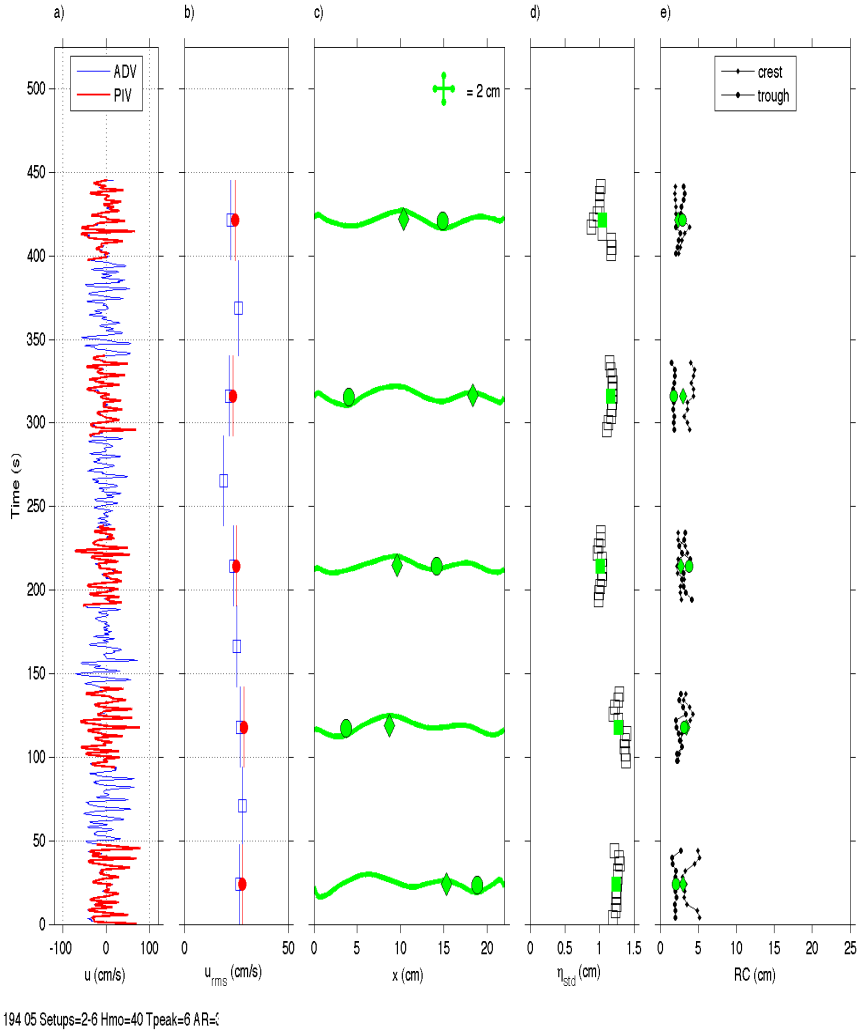

Figure A.25: Velocity and sea bed geometry resulting from 40 cm significant wave height and 8 second peak period. a) Velocity data as collected by the PIV system (red) and ADV (blue). b) Root-mean-square velocity over 48 second time intervals, using the same color scheme as a). 48 second average bed forms are depicted in c). Diamond and circular markers on each bed form reveal the location of the crest and trough locations used for RC measurements. d) Ripple height for 8 (black) and 48 (green) second average bedforms. e) RC measurements for 8 (black) and 48 (green) second average bedforms.

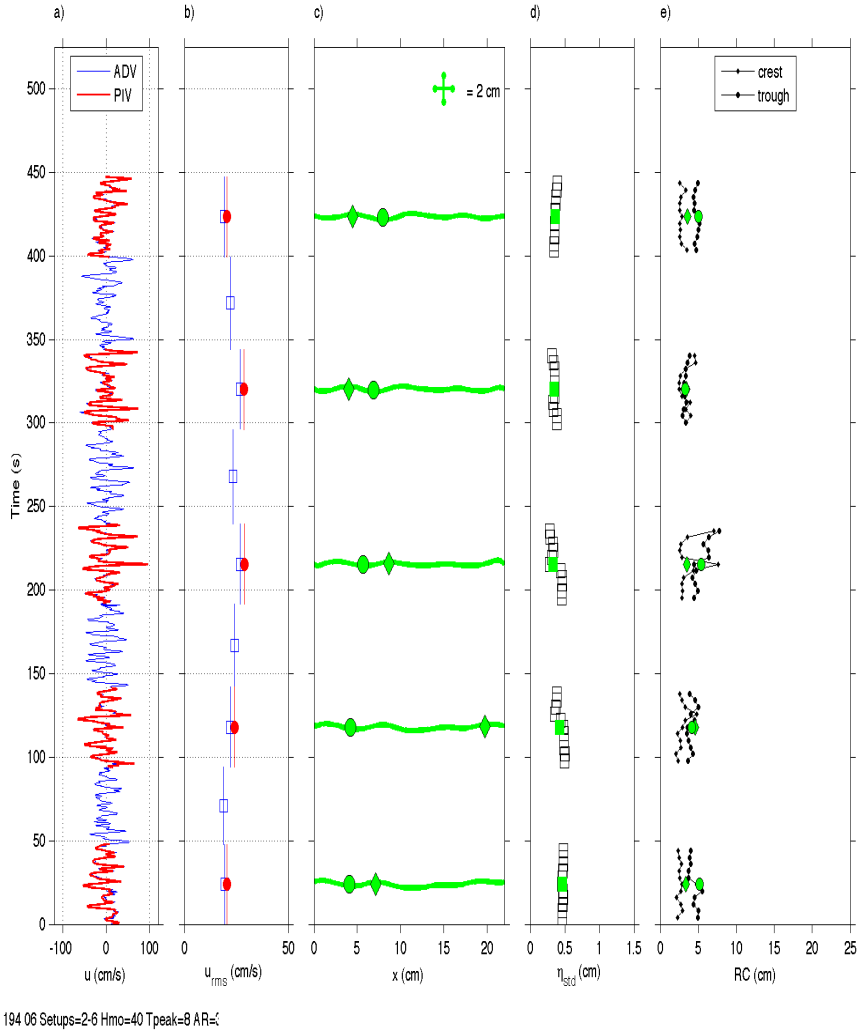

Figure A.26: Velocity and sea bed geometry resulting from 40 cm significant wave height and 8 second peak period. a) Velocity data as collected by the PIV system (red) and ADV (blue). b) Root-mean-square velocity over 48 second time intervals, using the same color scheme as a). 48 second average bed forms are depicted in c). Diamond and circular markers on each bed form reveal the location of the crest and trough locations used for RC measurements. d) Ripple height for 8 (black) and 48 (green) second average bedforms. e) RC measurements for 8 (black) and 48 (green) second average bedforms.

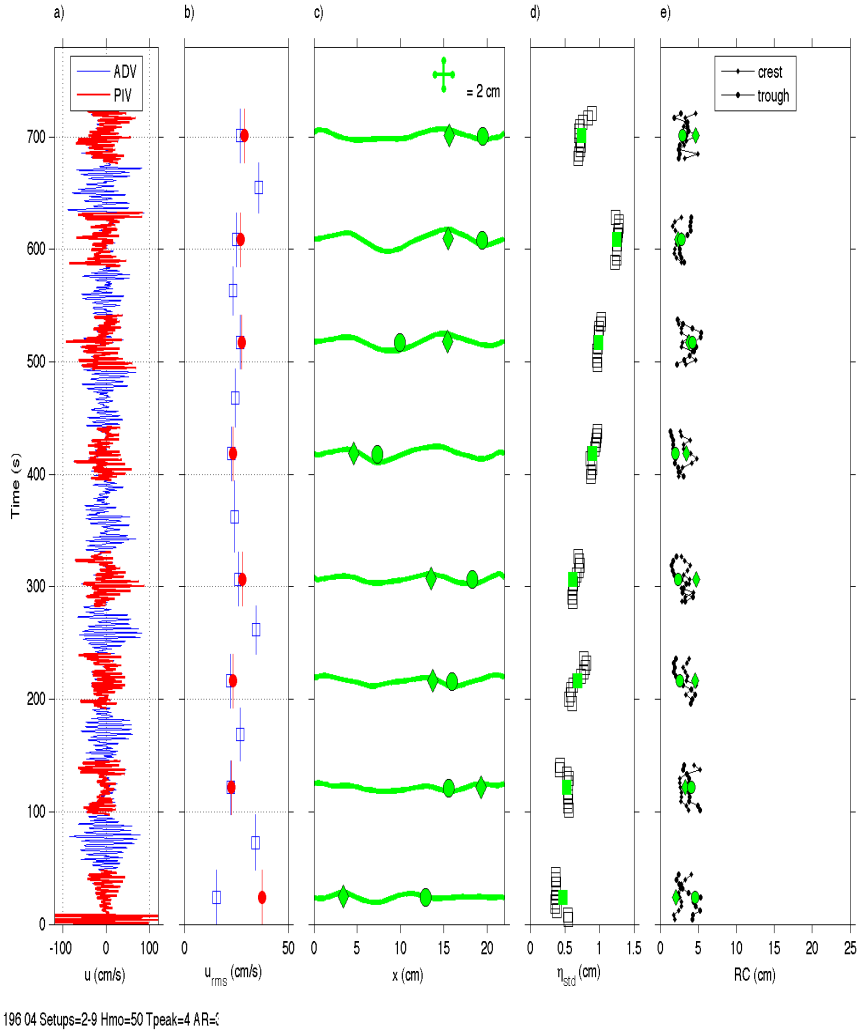

Figure A.27: Velocity and sea bed geometry resulting from 40 cm significant wave height and 8 second peak period. a) Velocity data as collected by the PIV system (red) and ADV (blue). b) Root-mean-square velocity over 48 second time intervals, using the same color scheme as a). 48 second average bed forms are depicted in c). Diamond and circular markers on each bed form reveal the location of the crest and trough locations used for RC measurements. d) Ripple height for 8 (black) and 48 (green) second average bedforms. e) RC measurements for 8 (black) and 48 (green) second average bedforms.

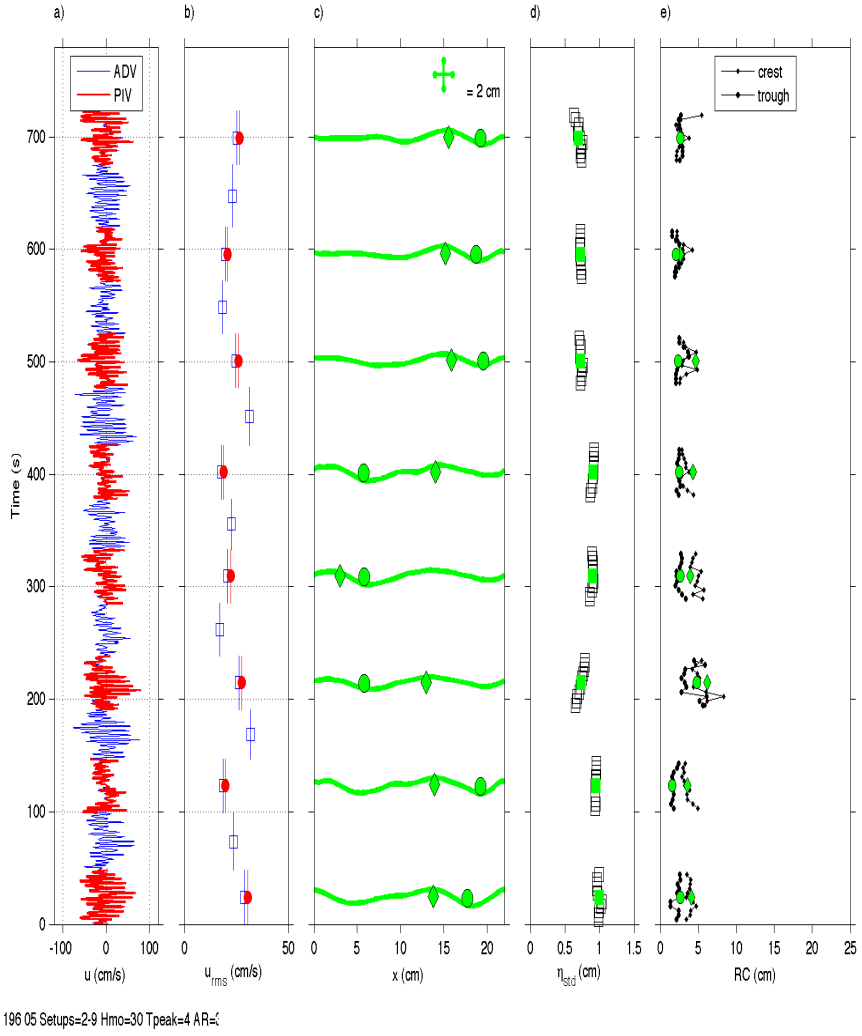

Figure A.28: Velocity and sea bed geometry resulting from 40 cm significant wave height and 8 second peak period. a) Velocity data as collected by the PIV system (red) and ADV (blue). b) Root-mean-square velocity over 48 second time intervals, using the same color scheme as a). 48 second average bed forms are depicted in c). Diamond and circular markers on each bed form reveal the location of the crest and trough locations used for RC measurements. d) Ripple height for 8 (black) and 48 (green) second average bedforms. e) RC measurements for 8 (black) and 48 (green) second average bedforms.

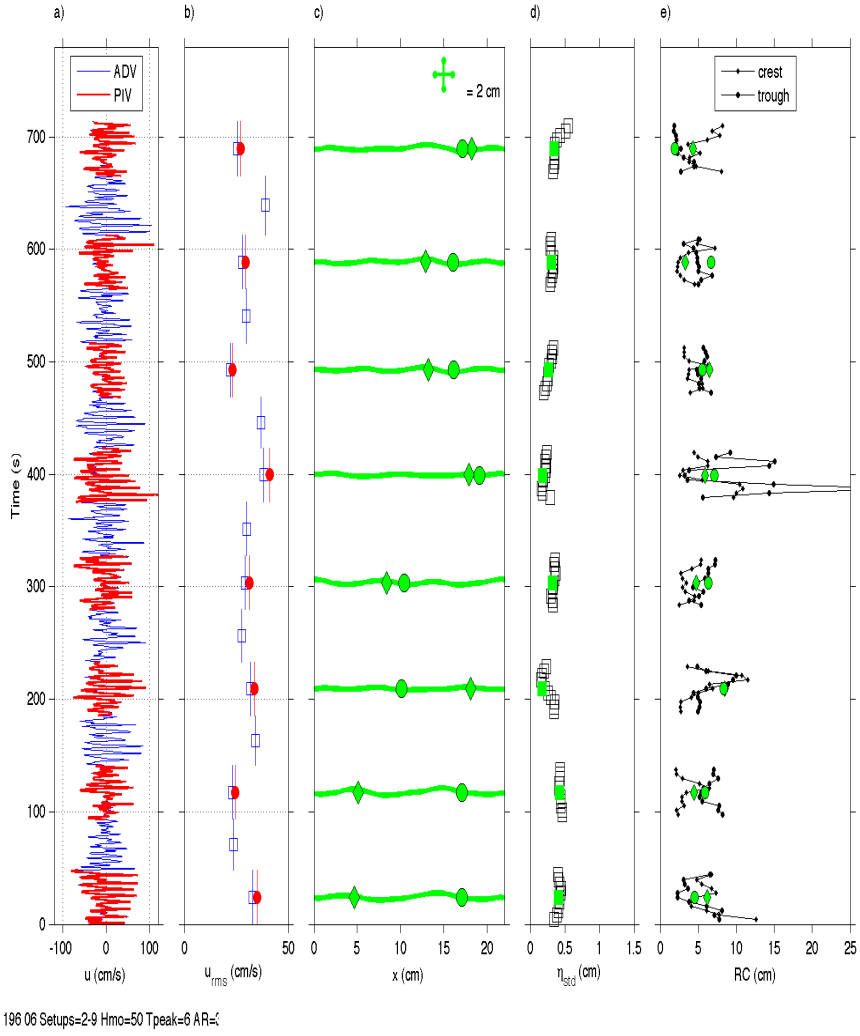

Figure A.29: Velocity and sea bed geometry resulting from 40 cm significant wave height and 8 second peak period. a) Velocity data as collected by the PIV system (red) and ADV (blue). b) Root-mean-square velocity over 48 second time intervals, using the same color scheme as a). 48 second average bed forms are depicted in c). Diamond and circular markers on each bed form reveal the location of the crest and trough locations used for RC measurements. d) Ripple height for 8 (black) and 48 (green) second average bedforms. e) RC measurements for 8 (black) and 48 (green) second average bedforms.

BIBLIOGRAPHY

Brown, J. (2006). Sea-bed response to non-breaking waves. *Undergraduate Honors Thesis - Ohio State University*.

Clifton, H. E. (1976). Wave-formed sedimentary structures – a conceptual model. *SEPM Soc Sediment. Geol.*, 24:126–148.

Clifton, H. E. and Dingler, J. R. (1984). Wave-formed structures and paleoenvironmental reconstruction. *Marine Geology*, 60:165–198.

Crawford, A. M. and Hay, A. E. (2001). Linear transition ripple migration and wave orbital velocity skewness. *J. Geophys. Res.*, 106:14,113–14,128.

Hay, A. E. and Mudge, T. (2005). Principal bed states during sandyduck97: Occurrence, spectral anisotropy, and the bed state storm cycle. *J. Geophys. Res.*, 110(C03013, doi:10.1029/2004JC002451):1–18.

Nichols, C. S. and Foster, D. L. (2007). Full-scale observations of wave-induced vortex generation over a rippled bed. *J. Geophys. Res.*, 112(C10015, doi:10.1029/2006JC003841):1–17.

Wiberg, P. L. and Harris, C. K. (1994). Ripple geometry in wave dominated environmentsf. *J. Geophys. Res.*, 99(C1):775–789.